GSA Data Repository 2016190

Data Repository Material for "Rapid variation in upper-mantle rheology across the San Andreas Fault system and Salton Trough, southernmost California"

DOI: 10.1130/G37847.1

Shahar Barak,[1] Simon L. Klemperer,[1]

Contents of this document

1. Criteria used in assignment of quality to shear-wave splitting measurements

For each measurement we assign a quality ("good", "fair" or "poor") based on the following five criteria: existence of one clear maximum, small size of the 95% confidence area, linearity of the corrected particle motion, waveform similarity of corrected wavelet, removal of energy on the component perpendicular to the initial polarization, and agreement between the RC, SC and EV in splitting parameters. A quality of "good" is assigned to measurements in which all criteria are met, "fair" to measurements in which most criteria are met, and "poor" to measurements in which only a few criteria are met. Figure DR2A shows the quantity and quality of measurements for each station we analyzed in Splitlab. Figures DR3 through DR5 show examples of "good", "fair" and "poor" measurements, respectively.

2. Testing for a two-layer anisotropic model

We observe modest variation in splitting parameters with back-azimuth in all our stations (Figures DR7 to DR55). Systematic variations of the splitting parameters with back-azimuth are diagnostic of complex anisotropy [*Silver and Savage*, 1994], and it is possible to test the probability of a two-layer model by inverting the splitting parameters [*Silver and Savage*, 1994; *Hartog and Schwartz*, 2001], although the inversion is highly non-unique [*Hartog and Schwartz*, 2001].

We perform a grid search on the range of possible values of the two-layer model parameters: ϕ_{upper}, δt_{upper}, ϕ_{lower}, δt_{lower}, and search for the model that minimizes the root-mean-square of the residual between the data and the predicted data. The predicted data is calculated using the equations of *Silver and Savage* [1994]. Because we have a limited range of backazimuths (Fig. DR1) we group stations based on the one-layer station-averaged fast polarizations (see Main). Only good and fair quality measurements are used. Because we only have a few measurements at each station, we resample the data with replacement (bootstrapping) 100 times prior to the inversion, to provide better constraints on the uncertainties. Since there is not a unique two-layer model that fits observed splitting parameters [*Hartog and Schwartz*, 2001], we show the distribution of the 100 models (Fig. DR6).

Our results, hindered by the limited range of backazimuths, show that a two-layer model is not statistically better than for a one-layer model. In addition to *Silver and Savage* [1994] and *Hartog and Schwartz* [2001], *Özalaybey and Savage* [1994, 1995] and *Bonnin et al.* [2010] have all successfully modeled two-layer anisotropy in Northern California, demonstrating the value of permanent stations to capture earthquakes with a broad range of back-azimuths. Similarly long-term recordings will be needed in southernmost California to properly test for multi-layer anisotropy. The dense network of broadband stations in southern California has allowed fully 3D anisotropic inversions [*Monteiller and Chevrot*, 2011; *Lin et al.*, 2014], and further south *Long* [2010] demonstrated the existence of vertical heterogeneity of anisotropy in the Gulf of California region, using the data of *Obrebski et al.* [2006]; *van Benthem et al.* [2008].

3. One-layer anisotropic model

We estimate the one-layer anisotropic model beneath each station by calculating a weighted mean and standard deviation (s.d.) for δt, and an axial weighted-mean and s.d. for ϕ [*Berens*, 2009]. We weight the mean by the quality of the measurements as follows: 1(good); 0.5(fair); 0.001(poor).

4. Caption for Figures DR3 through DR5

Figures DR3 through DR5 show examples of "good" "fair" and "poor" SWS measurements, respectively.
Top left: Radial (blue dashed) and transverse (red solid) components at the same vertical scale. Gray area: chosen window.
Top center: Summary of results as numerical values.
Top right: Polar diagram on which the fast polarization direction is plotted with the actual backazimuth and inclination.
Middle horizontal panel: Set of diagrams obtained by using the rotation-correlation (RC) method. From left to right: **a**, Fast (blue dashed) and slow (red solid) split components corrected from the delay time. **b**, Radial (blue) and transverse (red) components corrected from the anisotropy. This allows to see if the signal on the transverse component has been almost entirely removed after correction for the best ϕ and δt pair. **c**, Particle-motion diagram, before (blue) and after (red) the anisotropy correction. In case of a good measurement, the elliptical particle motion is essentially linear after the anisotropy (ϕ and δt) correction. **d**, Map of the correlation coefficients showing the quality of the correlation between the fast and slow split waves for ϕ varying from -90 to 90° and for δt varying from 0 to 4 s. Innermost contour shows 95% confidence interval.
Bottom horizontal panel: Set of diagrams obtained by

[1]Department of Geophysics, Stanford University, Stanford, California, USA.

using the minimum energy method [*Silver and Chan*, 1991]. From left to right: **a**, **b** and **c**, as for RC method. The particle motion diagram, before (in blue) and after (in red) the anisotropy correction. **d**, Map of the energy on transverse components.

5. Caption for Figure DR6

An example for the results of our two-layer inversion. In this example, we use our westernmost stations that exhibit a 079° average fast-direction and a 0.8 s mean delay time. **a:** Fast directions vs. backazimuth. Measurements (cross) colored by quality (magenta: good, green: fair). Blue dashed line: Best fit model. black line: one-layer average divided to two equal layers. **c–i**: Projections of the four-dimensional two-layer model parameter space onto seven different planes for the 100 models (cross), colored by the misfit. Blue square: best fit model (smallest misfit). Black circle: One-layer model.

6. Caption for Figures DR7 through DR55

SWS measurements for each station we analyzed. **a:** Fast polarization directions shown as thin black vectors with circles colored by quality (red for good, blue for fair, and green for poor) on a unit circle. Dashed magenta line ('AW' in legend): Quality-weighted axial mean calculated for all the measurements. Thick double-sided vectors: Axial mean calculated for each category of quality, colored respectively. Length of double-sided vectors proportional to the circular spread of the data. The closer it is to one, the more concentrated the data sample is around the mean direction. **b:** as in (**a**), but categorized by method instead of quality. RC stands for Rotation Correlation (red), SC for Silver and Chan (Energy Minimization, blue), and EV for Eigenvalue (green) [*Wüstefeld et al.*, 2008]. **c:** Fast polarization direction vs. backazimuth, colored by quality, as in (**a**). **d:** Delay time vs. backazimuth, colored by quality, as in (**a**).

7. Caption for Data Set DR1

Text file with statistics for each station we analyzed. The first 46 stations are part of our bbSSIP array. The 4 remaining stations, are those analyzed to test the method we used against results from a different method. The count of good, fair and poor events, are shown in columns 2–4, respectively. The weighted axial-mean and weighted standard deviation of the fast polarization directions and weighted mean and weighted standard deviation of the delay times are shown in columns 5–8, respectively. Please note that results from our stations A07 and A07A, and similarly for stations A26 and A26A, were combined. Also, stations A17 and B03 did not produce any reliable measurements.

8. Caption for Data Set DR2

Text file with all our splitting measurements. The year, day-of-year, phase, backazimuth, and inclination of the earthquake are shown in columns 2 through 6. The low and high frequency cut offs are shown in columns 7 and 8, respectively. The fast polarization direction and time delay for each method are shown in columns 9 through 14. The final column shows our assigned quality.

References

Berens, P. (2009), CircStat : A MATLAB Toolbox for Circular Statistics, *Journal of Statistical Software*, *31*(10), 1–21, doi: 10.18637/jss.v031.i10.

Bonnin, M., G. Barruol, and G. H. R. Bokelmann (2010), Upper mantle deformation beneath the North American-Pacific plate boundary in California from SKS splitting, *Journal of Geophysical Research*, *115*(B4), B04,306, doi: 10.1029/2009JB006438.

Chuang, R. Y., and K. M. Johnson (2011), Reconciling geologic and geodetic model fault slip-rate discrepancies in Southern California: Consideration of nonsteady mantle flow and lower crustal fault creep, *Geology*, *39*(7), 627–630, doi: 10.1130/G32120.1.

Field, E., G. Biasi, P. Bird, T. Dawson, K. Felzer, D. Jackson, K. Johnson, T. Jordan, C. Madden, A. Michael, K. Milner, M. Page, T. Parsons, P. Powers, B. Shaw, W. Thatcher, I. Weldon, R.J., and Y. Zeng (2013), Uniform California earthquake rupture forecast, version 3 (UCERF3)The time-independent model: U.S. Geological Survey Open-File Report 20131165.

Hartog, R., and S. Y. Schwartz (2001), Depth-dependent mantle anisotropy below the San Andreas fault system: Apparent splitting parameters and waveforms, *Journal of Geophysical Research*, *106*(B3), 4155, doi:10.1029/2000JB900382.

Kinsella, A., S. Barak, and S. Klemperer (2013), Rapid lateral variation of seismic anisotropy across the Salton Trough, Southern California, in *AGU Fall meeting, NH41B-1707*.

Lin, Y.-p., L. Zhao, and S.-h. Hung (2014), Full-wave multiscale anisotropy tomography in Southern California, *Geophysical Research Letters*, *41*(24), 8809–8817, doi: 10.1002/2014GL061855.

Long, M. D. (2010), Frequency-dependent shear wave splitting and heterogeneous anisotropic structure beneath the Gulf of California region, *Physics of the Earth and Planetary Interiors*, *182*(12), 59–72, doi:10.1016/j.pepi.2010.06.005.

Monteiller, V., and S. Chevrot (2011), High-resolution imaging of the deep anisotropic structure of the San Andreas Fault system beneath southern California, *Geophysical Journal International*, *186*(2), 418–446, doi:10.1111/j.1365-246X.2011.05082.x.

Obrebski, M., R. R. Castro, R. W. Valenzuela, S. van Benthem, and C. J. Rebollar (2006), Shear-wave splitting observations at the regions of northern Baja California and southern Basin and range in Mexico, *Geophysical Research Letters*, *33*(5), 2–5, doi:10.1029/2005GL024720.

Özalaybey, S., and M. K. Savage (1994), Double-layer anisotropy resolved from S phases, *Geophysical Journal International*, *117*(3), 653–664, doi:10.1111/j.1365-246X.1994.tb02460.x.

Özalaybey, S., and M. K. Savage (1995), Shear-wave splitting beneath western United States in relation to plate tectonics, *Journal of Geophysical Research*, *100*(B9), 18,135, doi: 10.1029/95JB00715.

Silver, P. G., and W. W. Chan (1991), Shear wave splitting and subcontinental mantle deformation, *Journal of Geophysical Research*, *96*(B10), 16,429, doi:10.1029/91JB00899.

Silver, P. G., and M. K. Savage (1994), The Interpretation of Shear-Wave Splitting Parameters In the Presence of Two Anisotropic Layers, *Geophysical Journal International*, *119*(3), 949–963, doi:10.1111/j.1365-246X.1994.tb04027.x.

van Benthem, S. a. C., R. W. Valenzuela, M. Obrebski, and R. R. Castro (2008), Measurements of upper mantle shear wave anisotropy from stations around the southern Gulf of California, *Geofisica Internacional*, *47*(2), 127–144.

Wüstefeld, A., G. Bokelmann, C. Zaroli, and G. Barruol (2008), SplitLab: A shear-wave splitting environment in Matlab, *Computers & Geosciences*, *34*(5), 515–528, doi: 10.1016/j.cageo.2007.08.002.

Corresponding author: S. Klemperer, Department of Geophysics, Stanford University, Mitchell Building 324, Stanford, CA 94305, USA. (sklemp@stanford.edu)

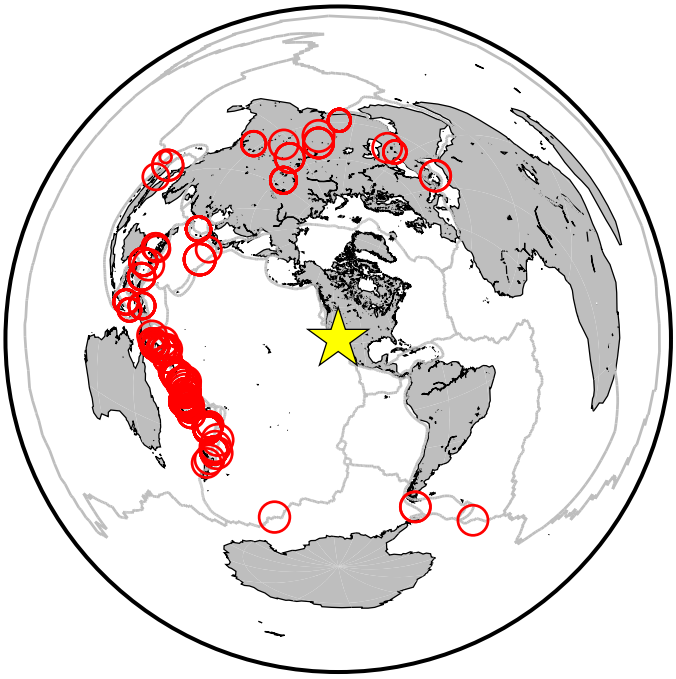

Figure DR1: Map of earthquakes (red circles) that yielded at least one SKS splitting measurement. Most earthquakes originate in the west and southwest Pacific. Yellow star: approximate center of our bbSSIP array.

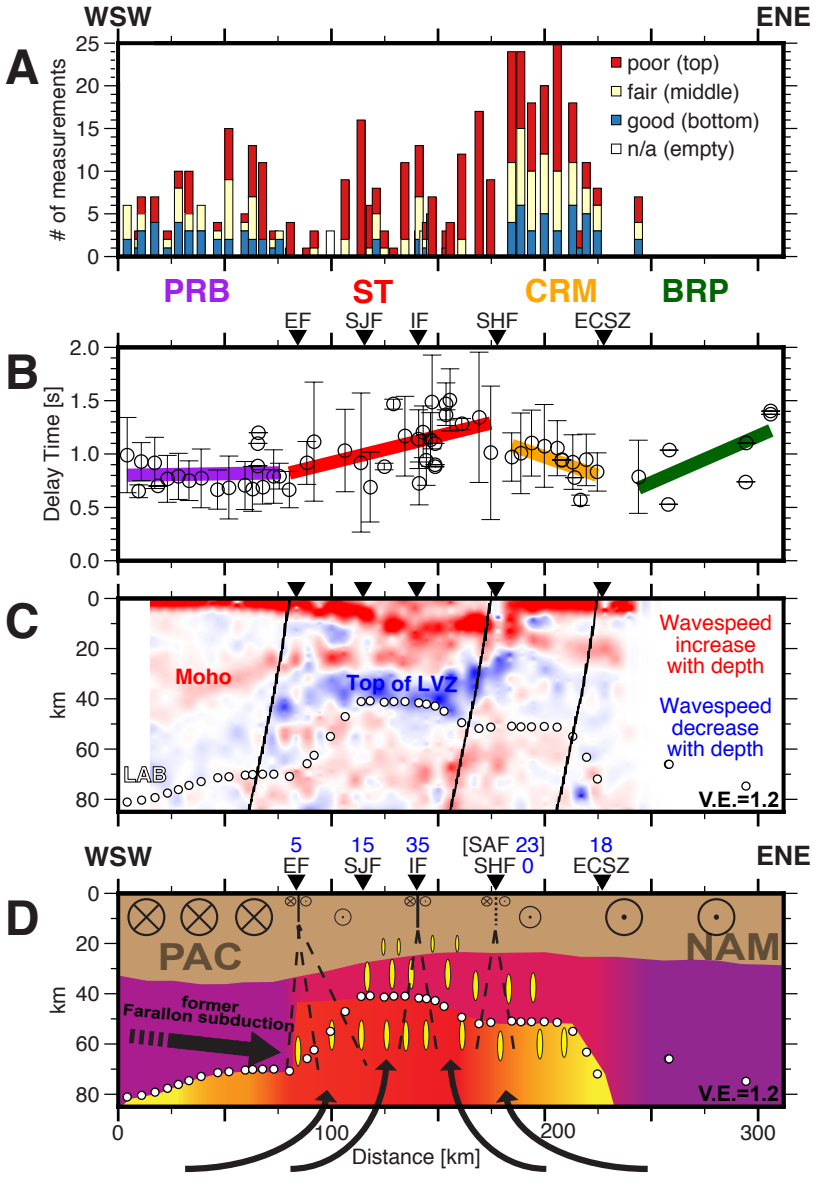

Figure DR2: **A:** Number of SWS measurements at each station, colored by quality ("good": blue; "fair": yellow; "poor": red; n/a: white), projected along the solid white line in Figure 1B. **B:** Mean delay time for each station (black circles), projected as in part A. Error bars are quality-weighted standard deviations. Other annotations as in Figure 2A. **C:** Ps receiver-function common-conversion-point image [*Kinsella et al.*, 2013]. Shallow red converter represents the sedimentary basin, deeper red converter the Moho, and blue converter the asthenospheric low-velocity zone. **D:** Tectonic cartoon. Numbers above each fault symbol are maximum estimates of geodetic fault slip rates, mm/yr [*Chuang and Johnson*, 2011; *Field et al.*, 2013]. Yellow ovals: aligned melt channels. Black curved arrows: upwelling mantle. Black dashed lines: inferred shear zones. ⊗ and ⊙: block motions into and out of the page, size crudely scaled to velocity with respect to EF.

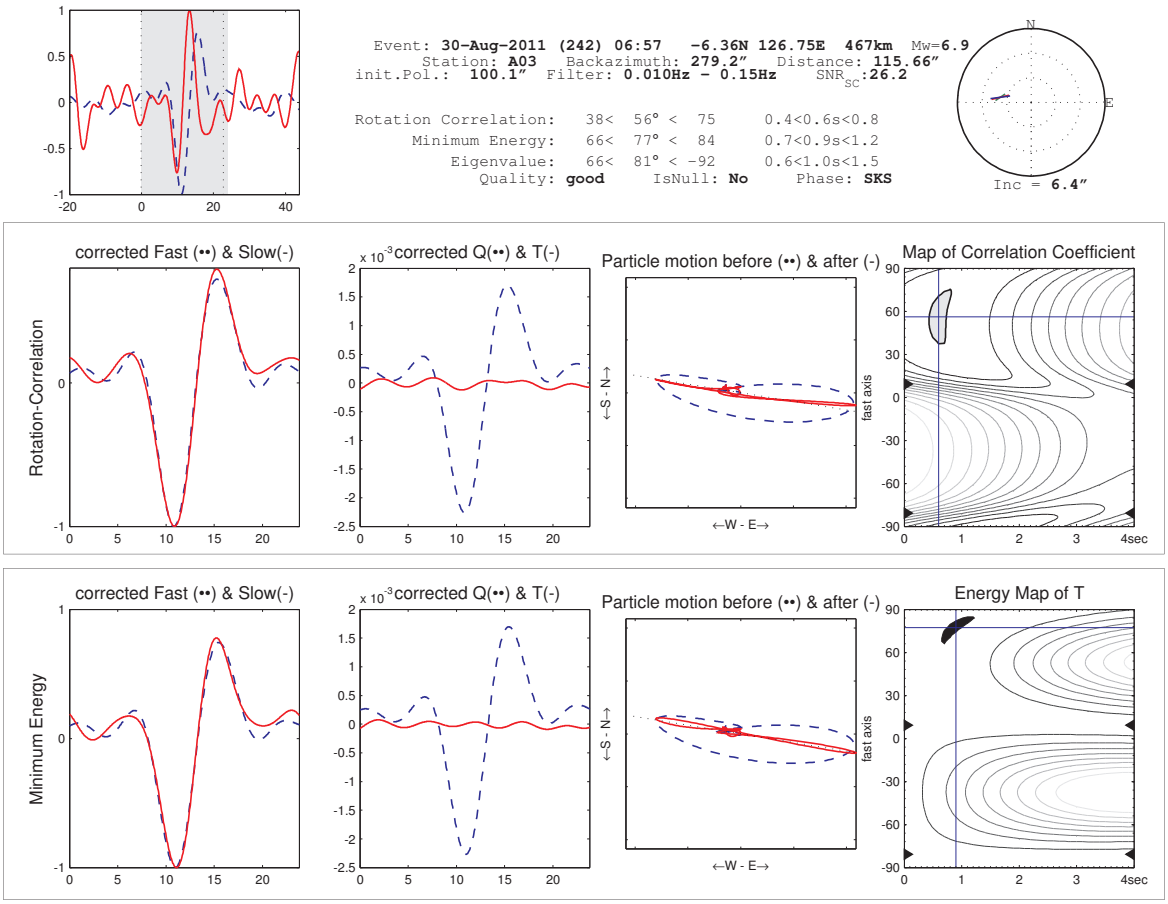

Figure DR3: Example of a "good" measurement. See detailed caption in the beginning of this document.

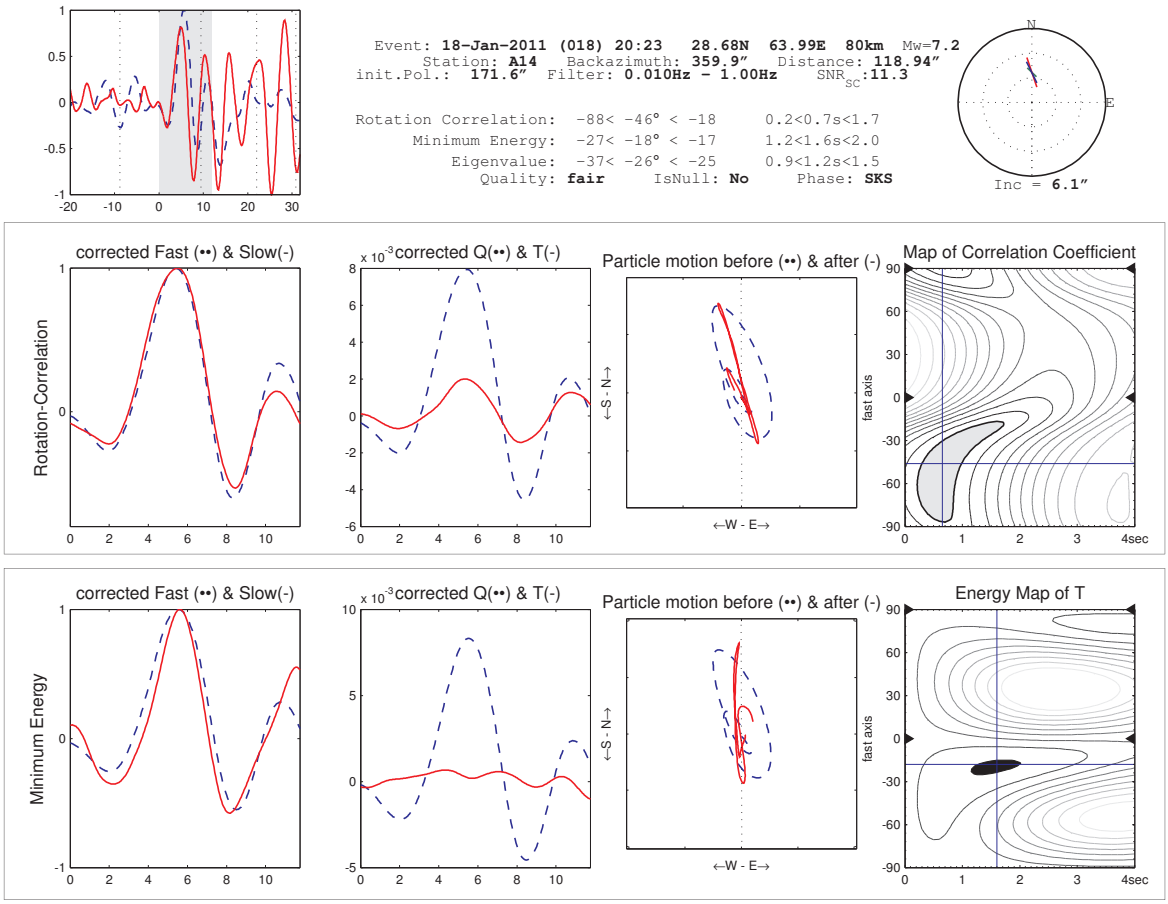

Figure DR4: Example of a "fair" measurement. See detailed caption in the beginning of this document.

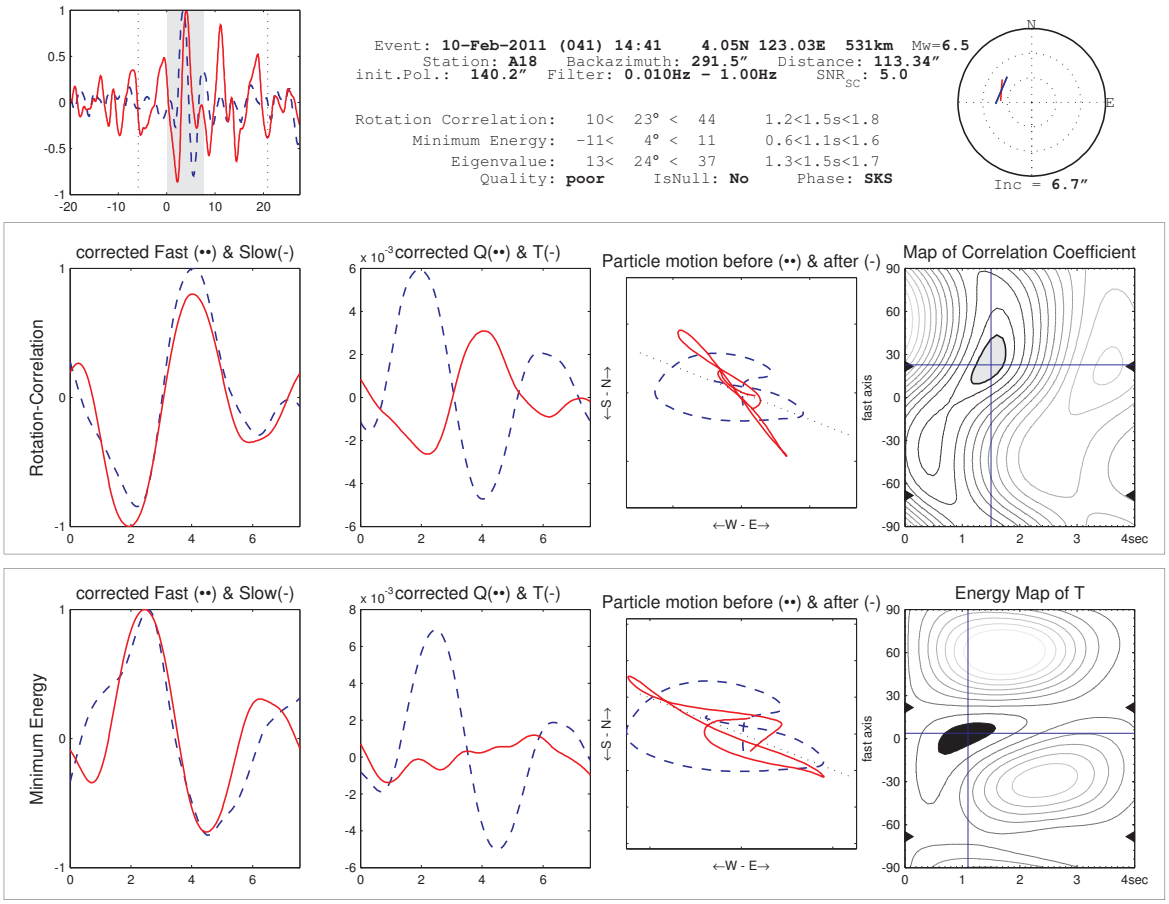

Figure DR5: Example of a "poor" measurement. See detailed caption in the beginning of this document.

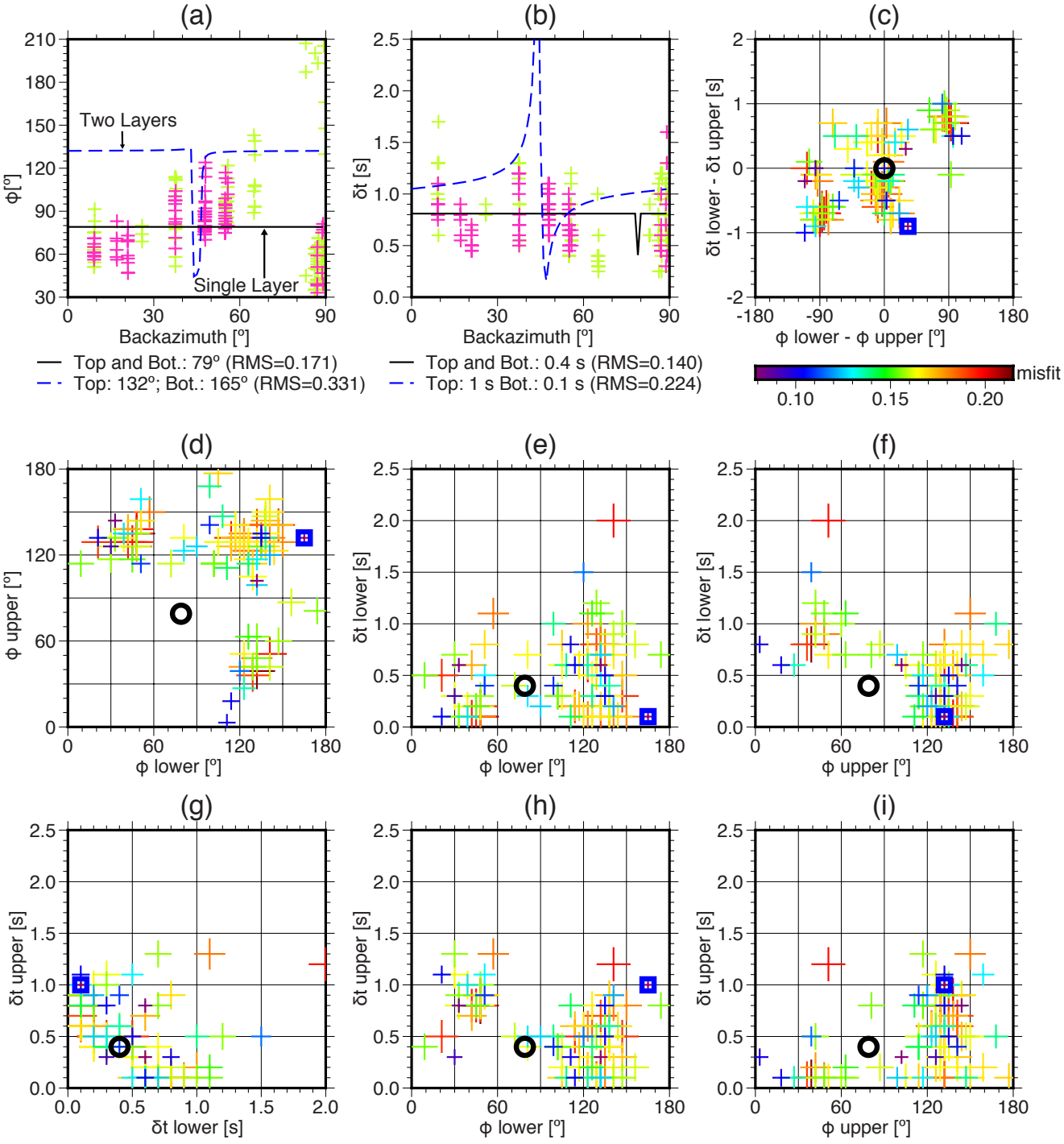

Figure DR6: Example for the results of our two-layer inversion. In this example, we show our westernmost stations that exhibit a 79° average fast-direction and a 0.8 s mean delay time. See detailed caption in the beginning of this document.

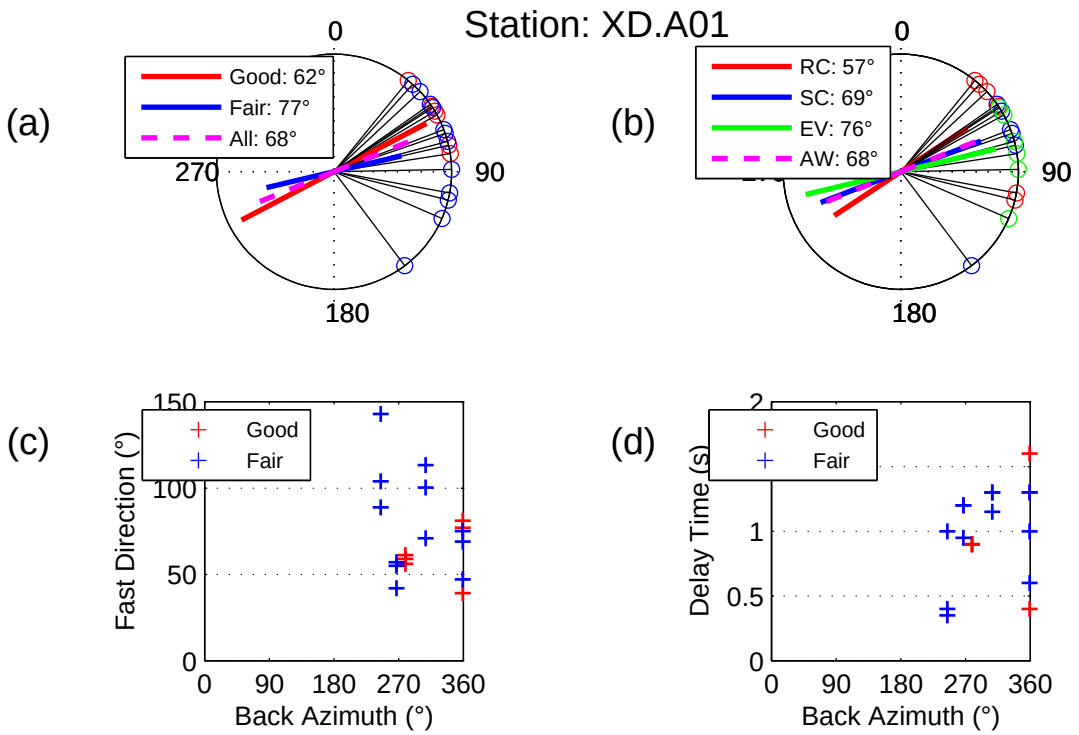

Figure DR7

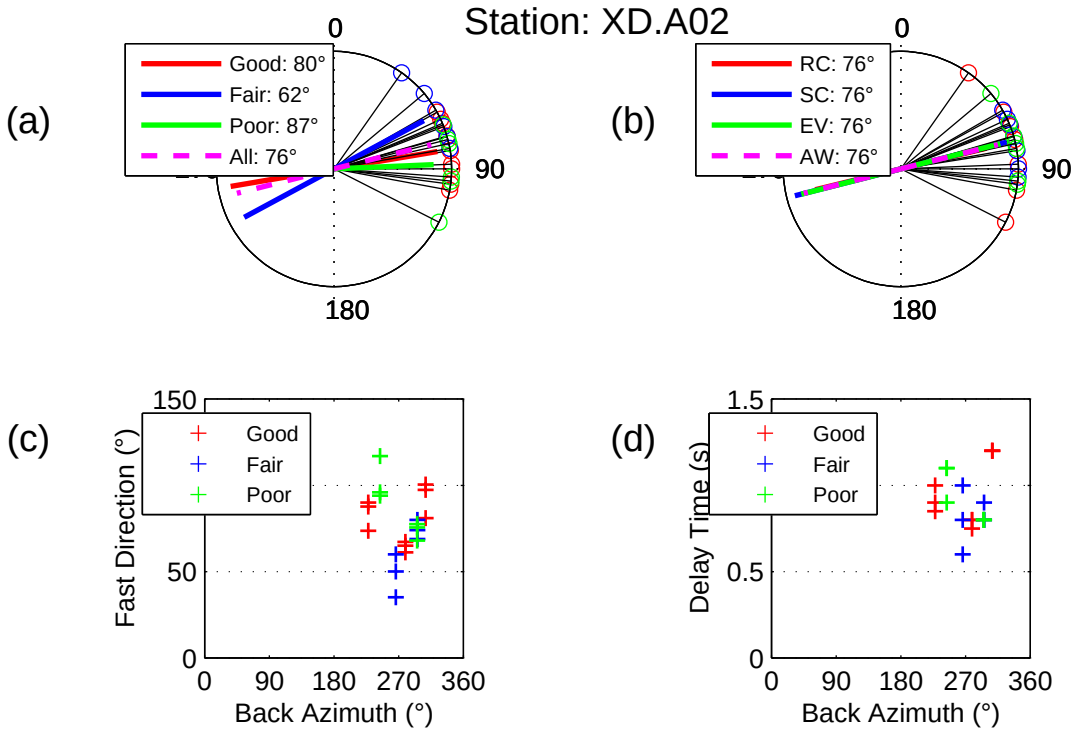

Figure DR8

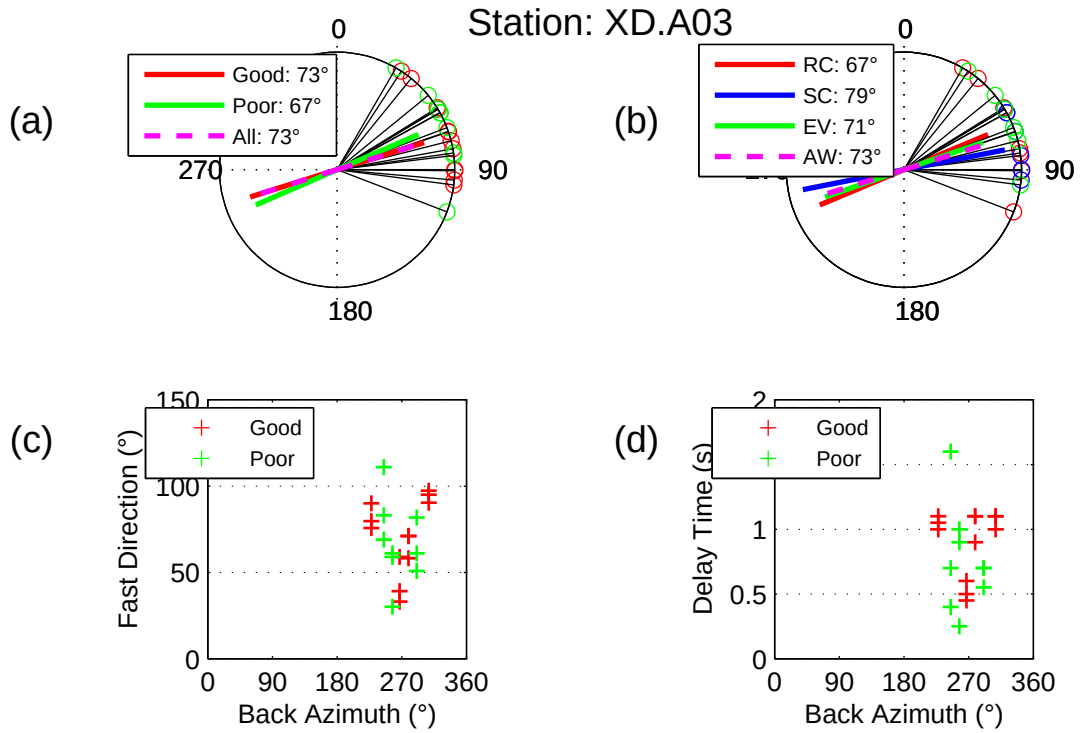

Figure DR9

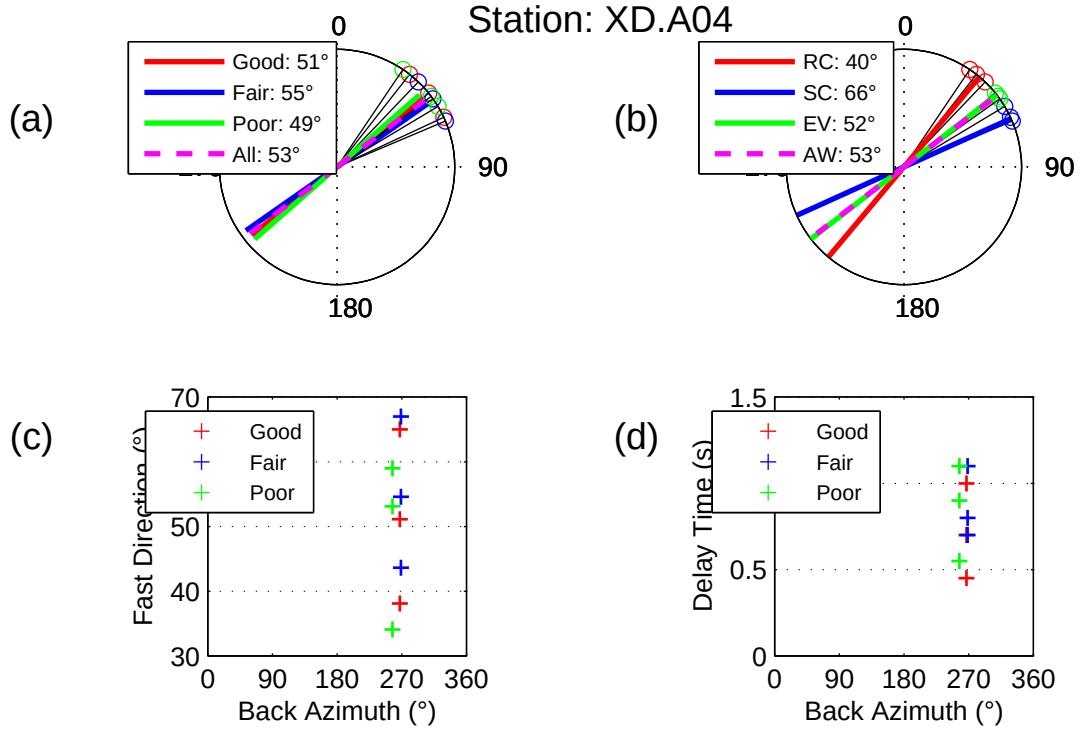

Figure DR10

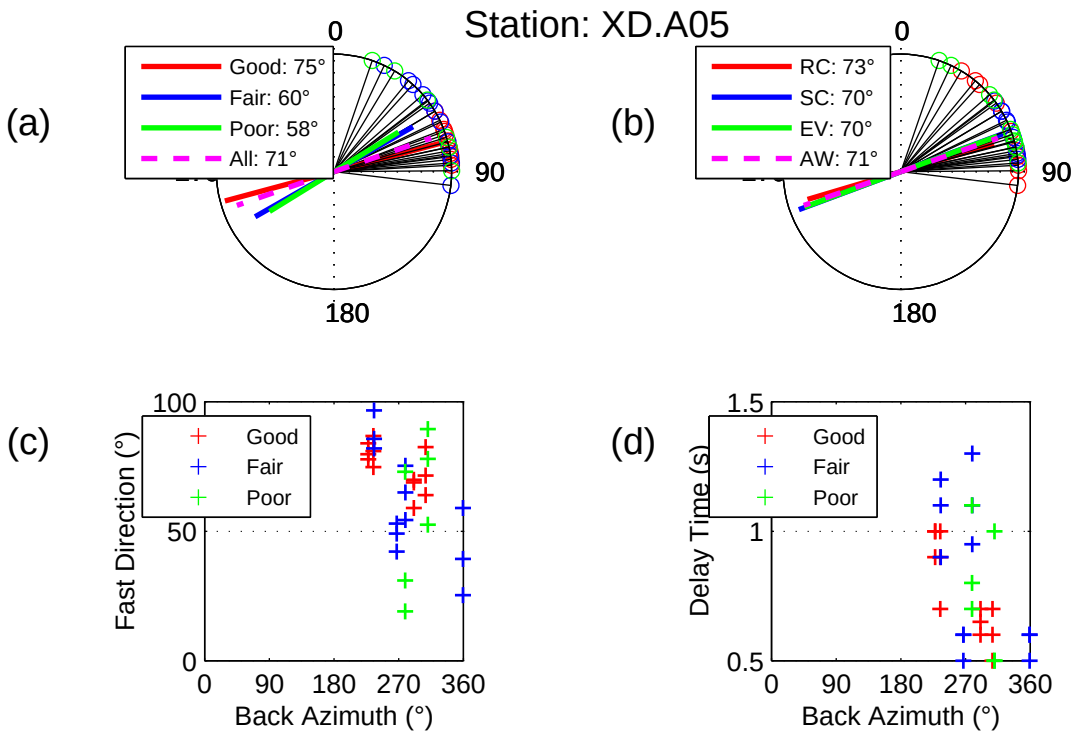

Figure DR11

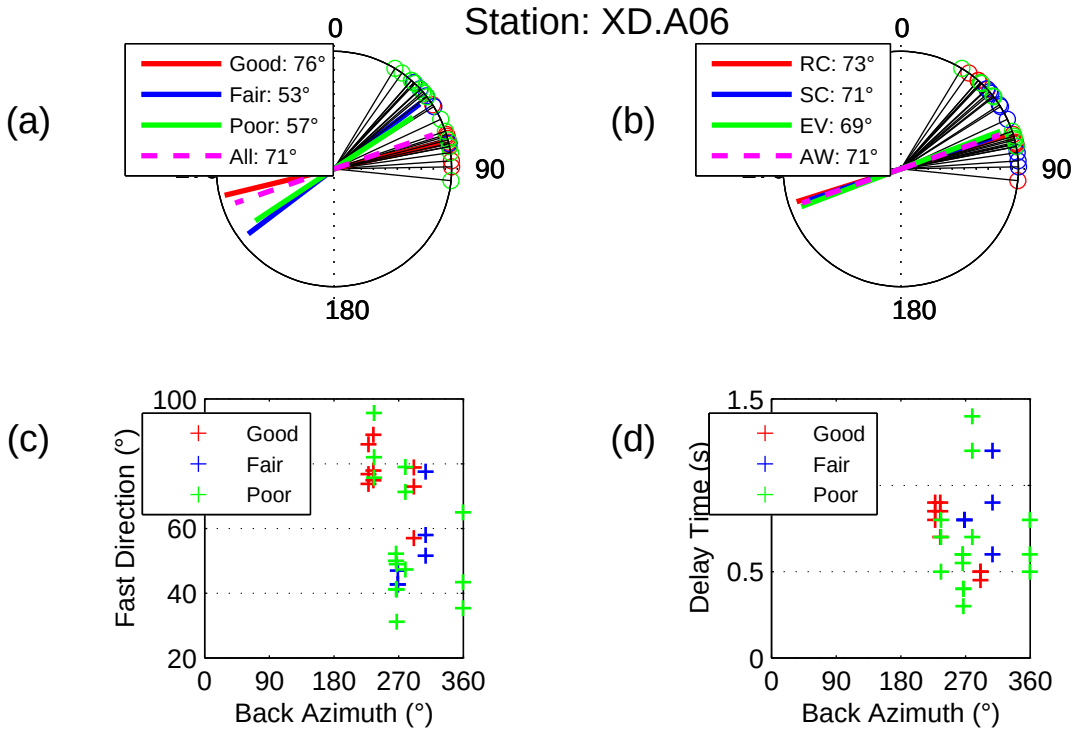

Figure DR12

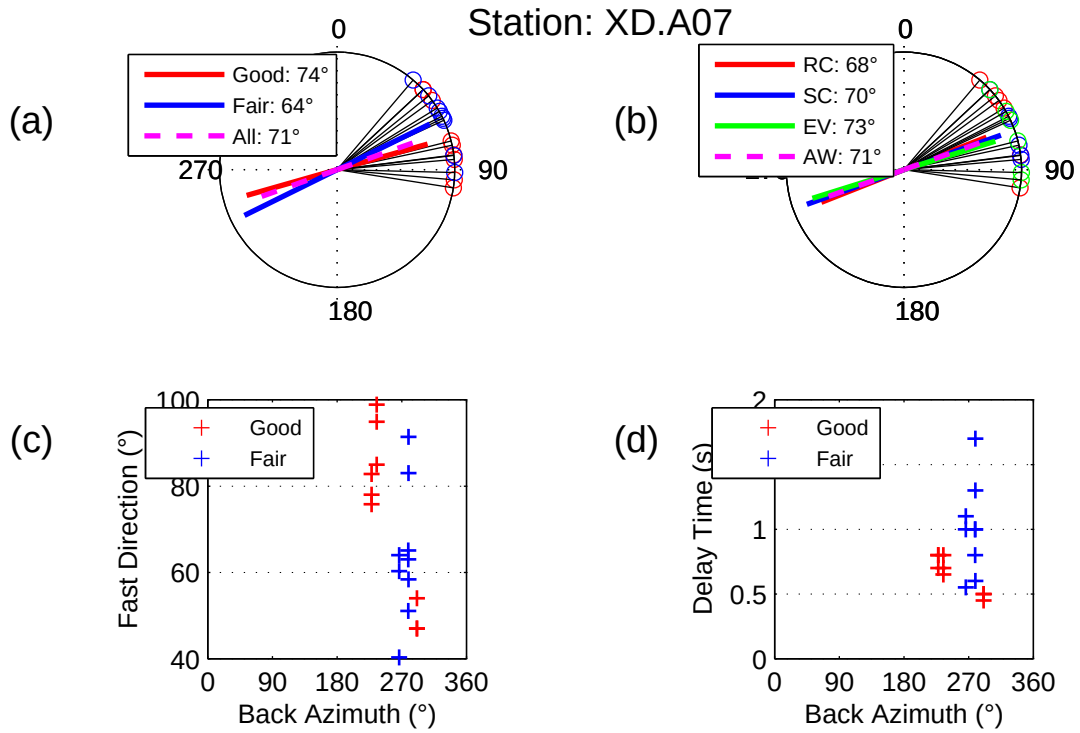

Figure DR13

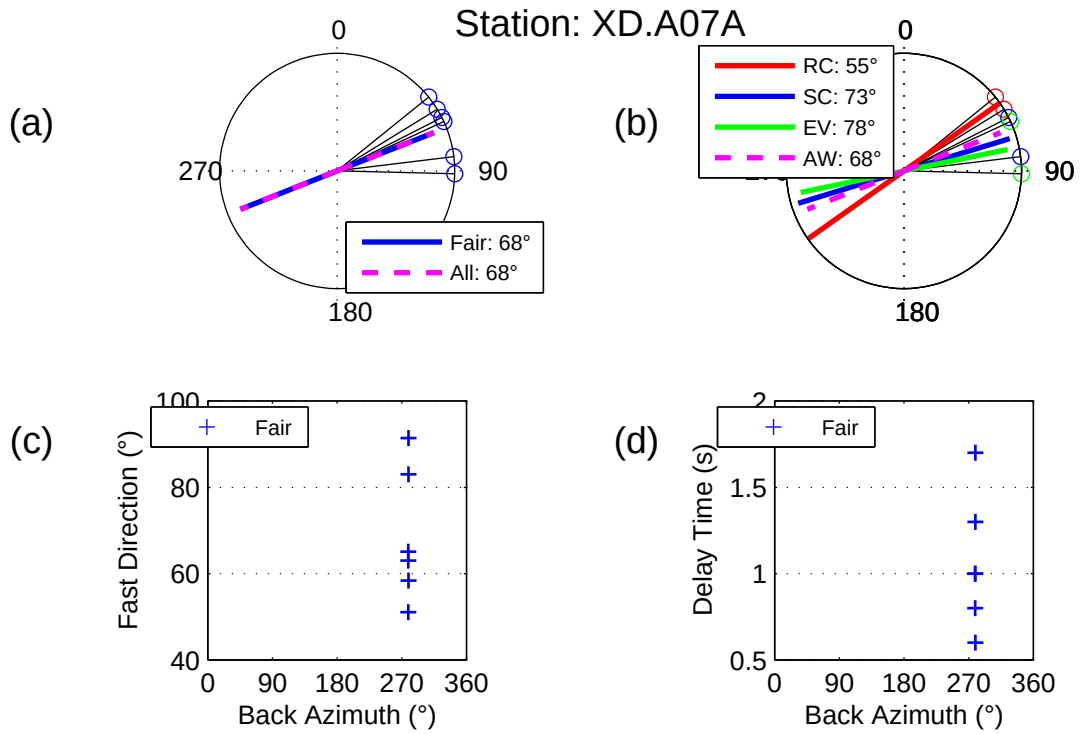

Figure DR14

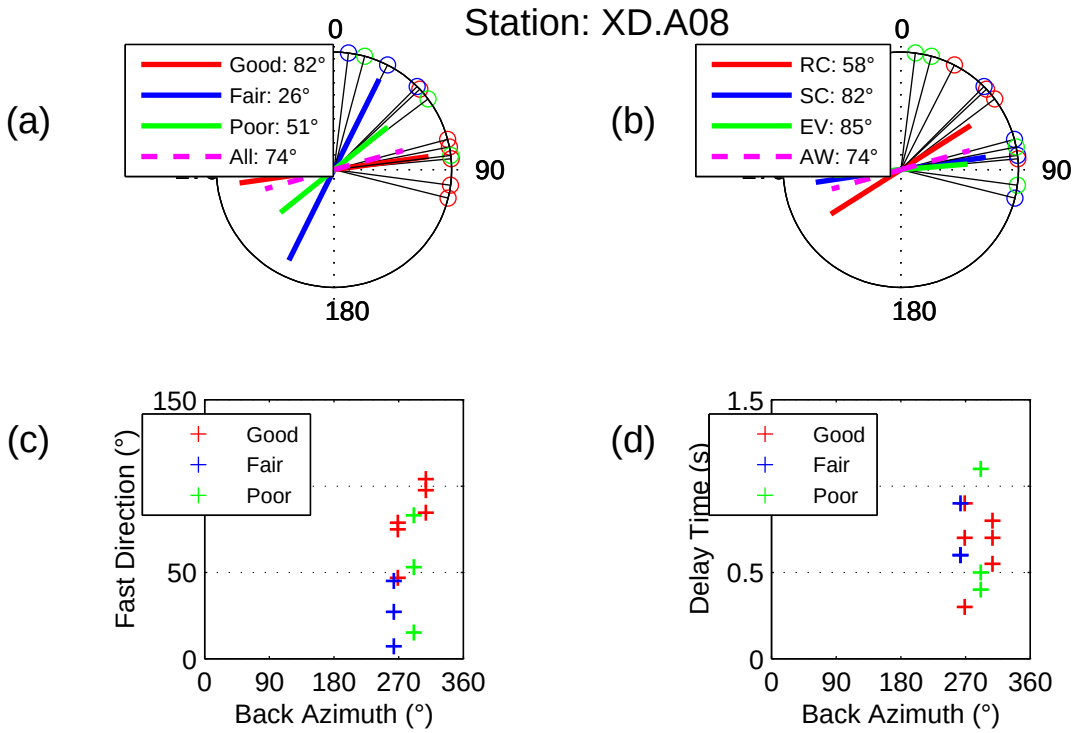

Figure DR15

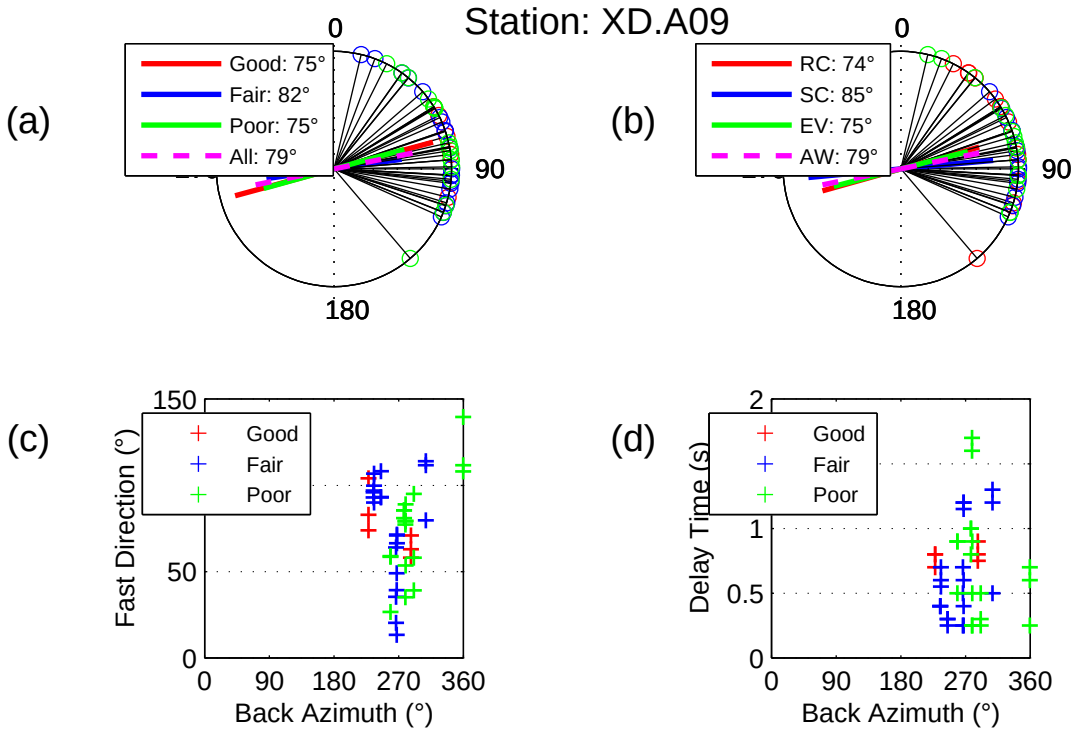

Figure DR16

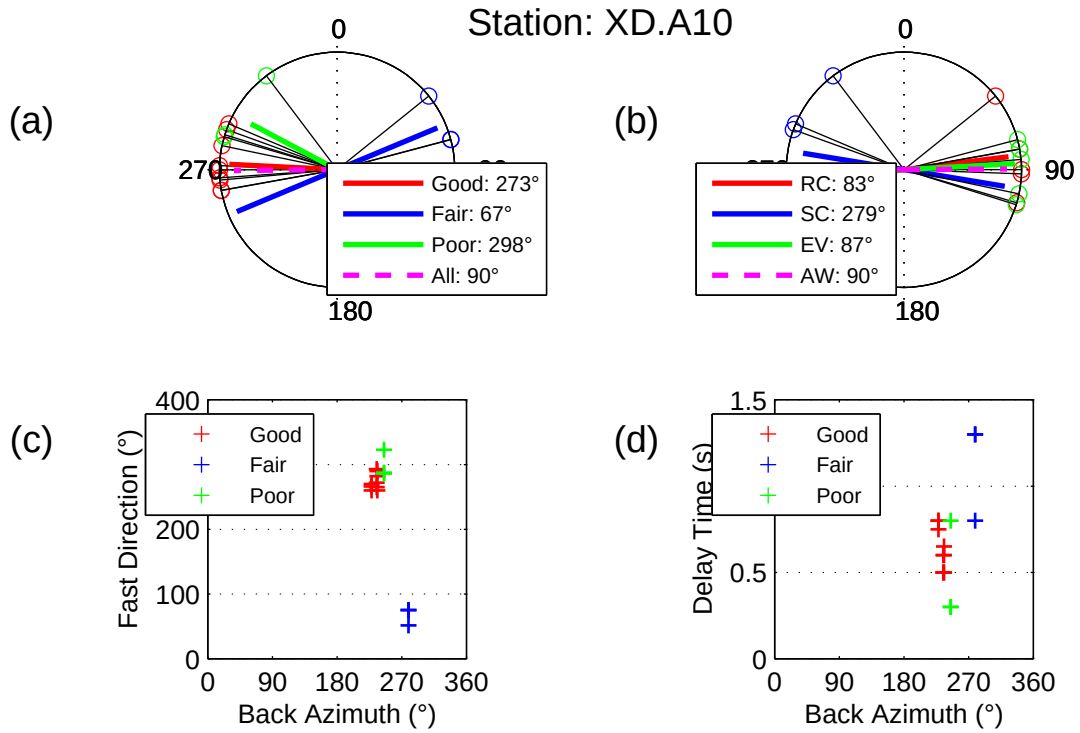

Figure DR17

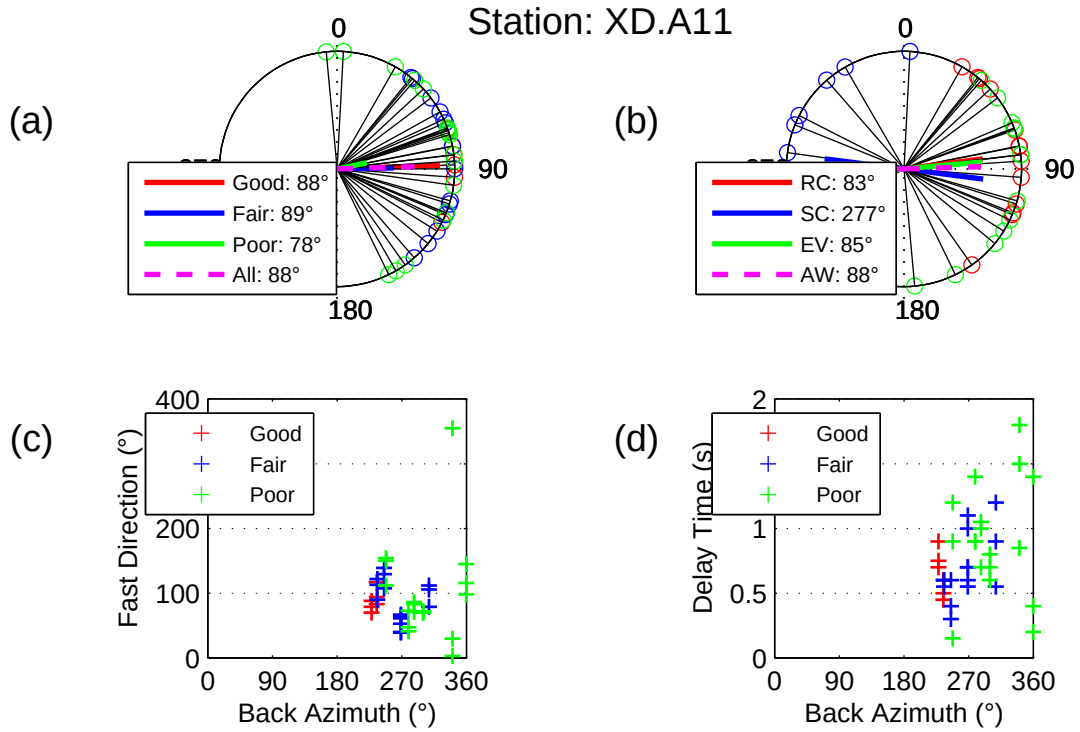

Figure DR18

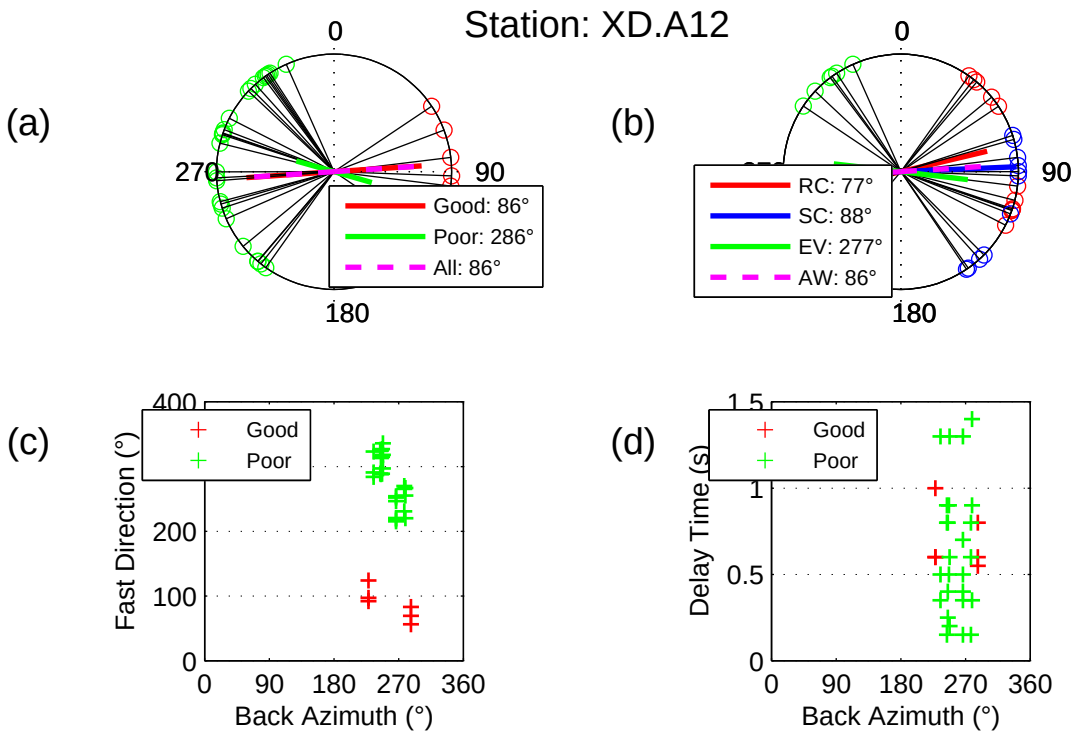

Figure DR19

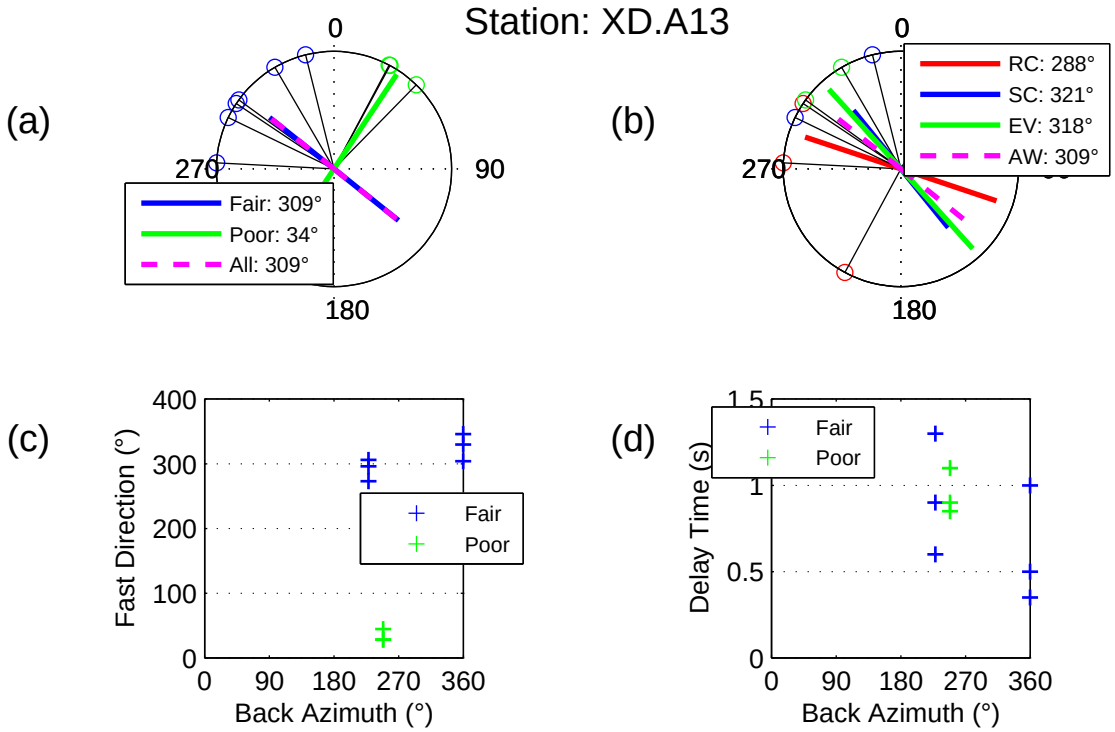

Figure DR20

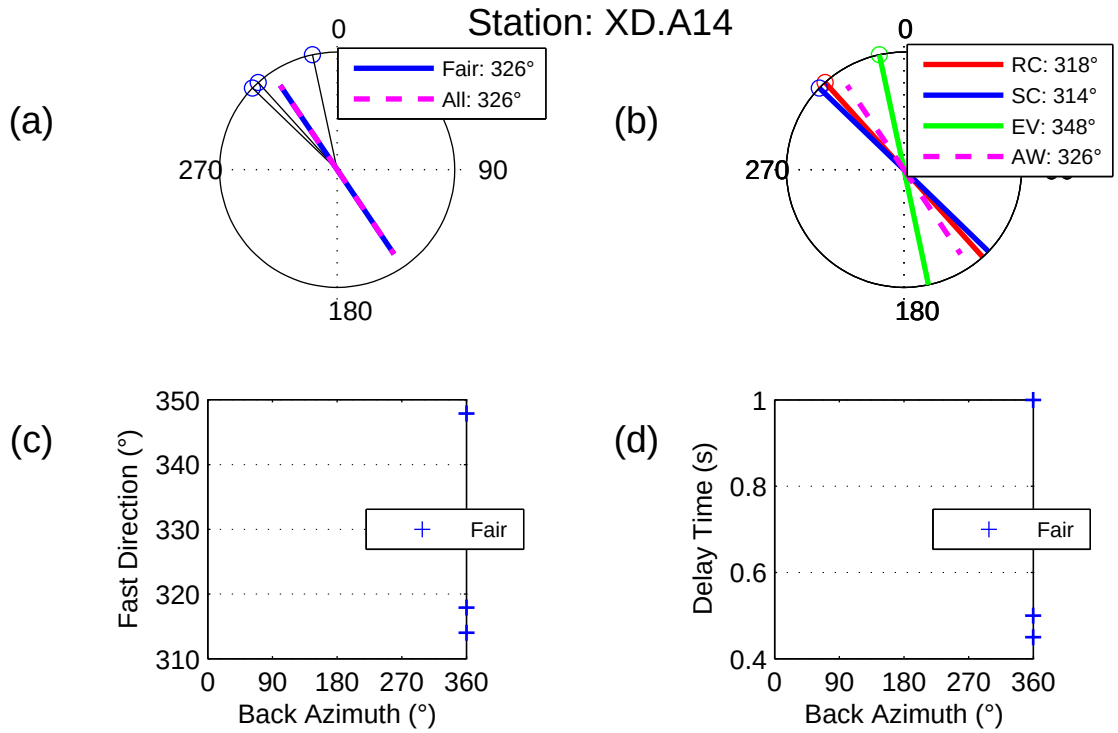

Figure DR21

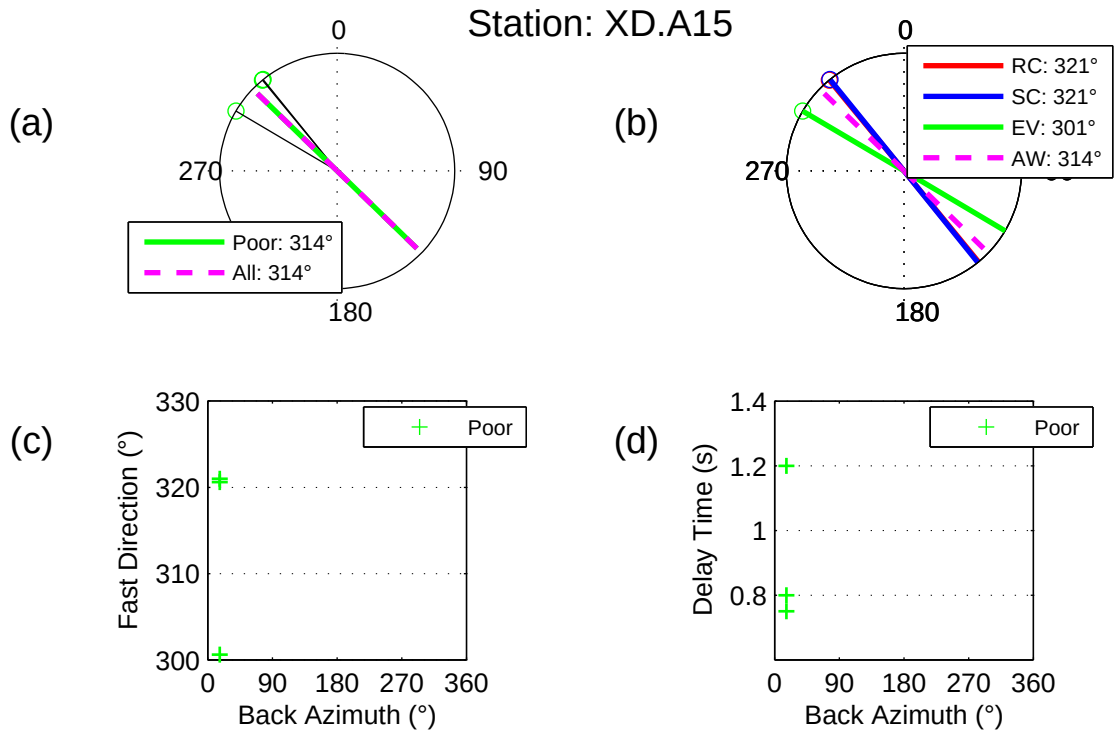

Figure DR22

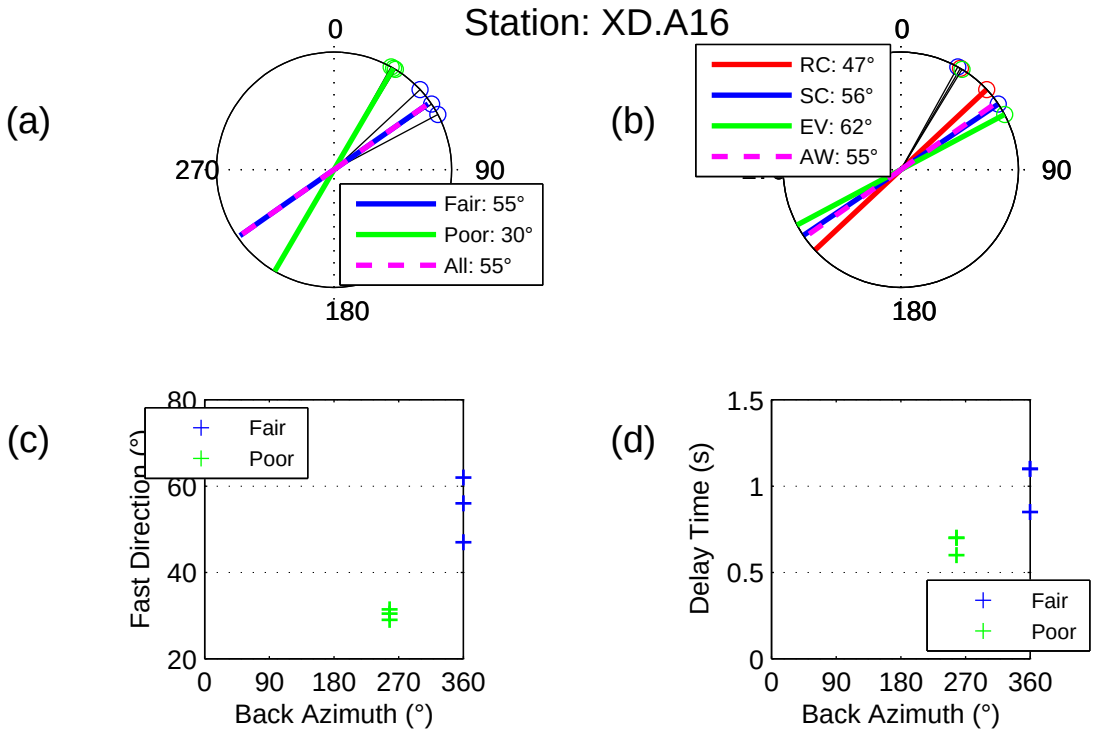

Figure DR23

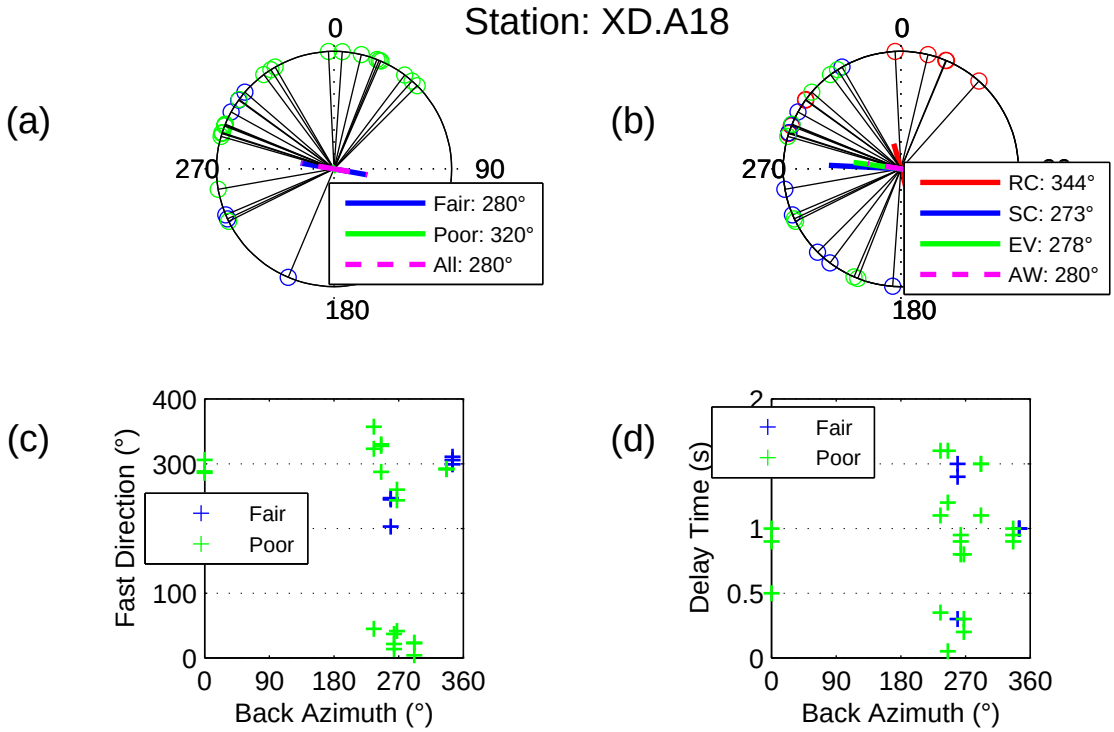

Figure DR24

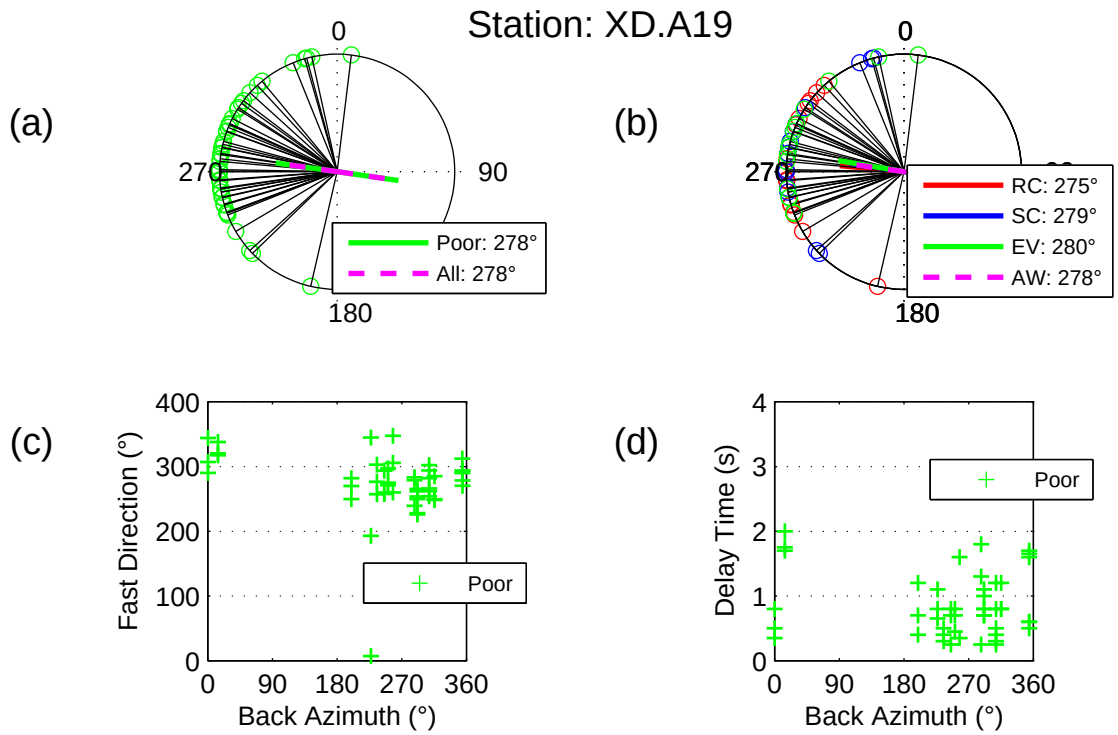

Figure DR25

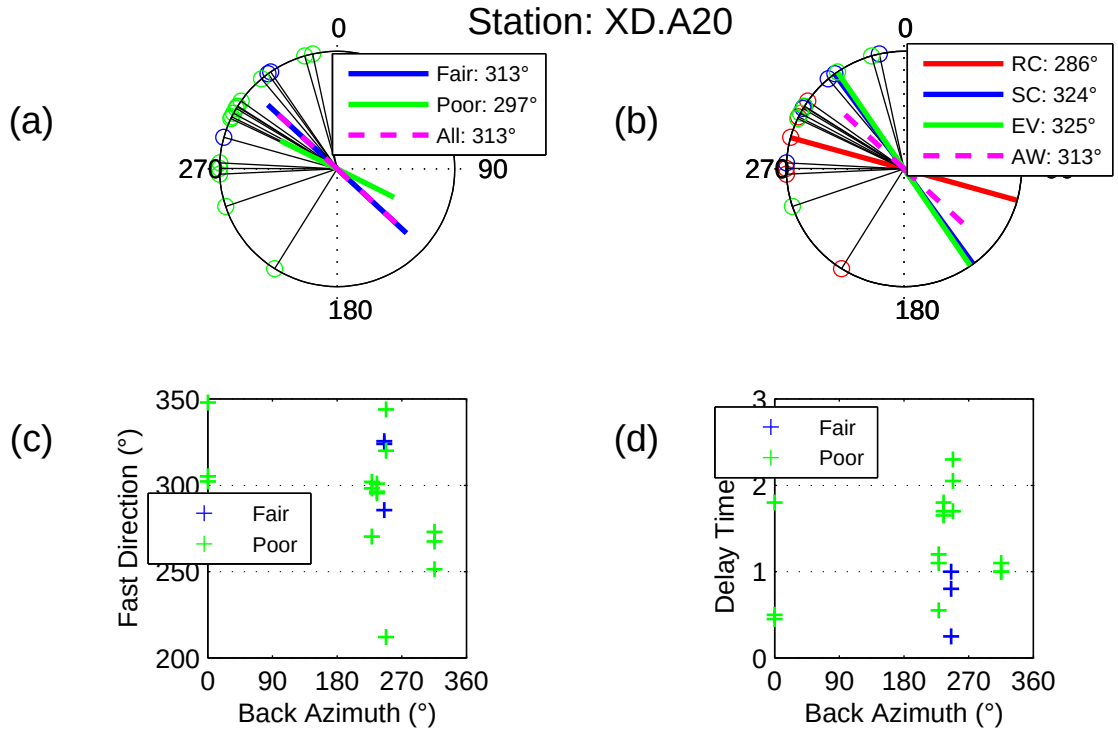

Figure DR26

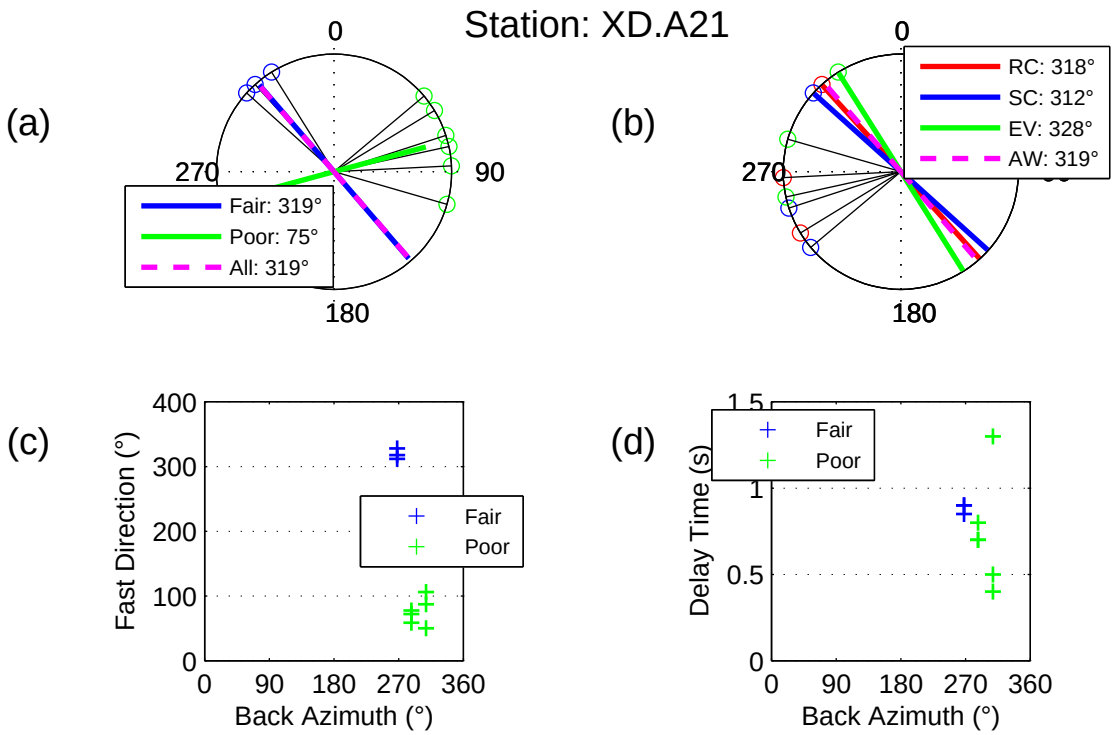

Figure DR27

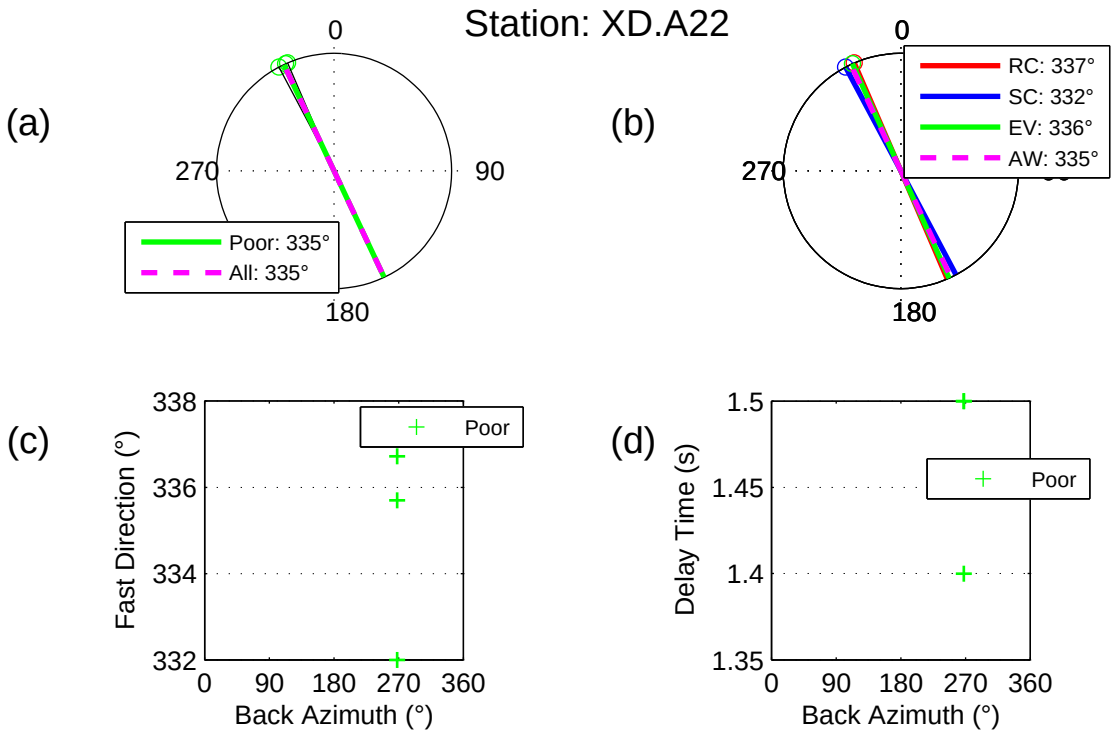

Figure DR28

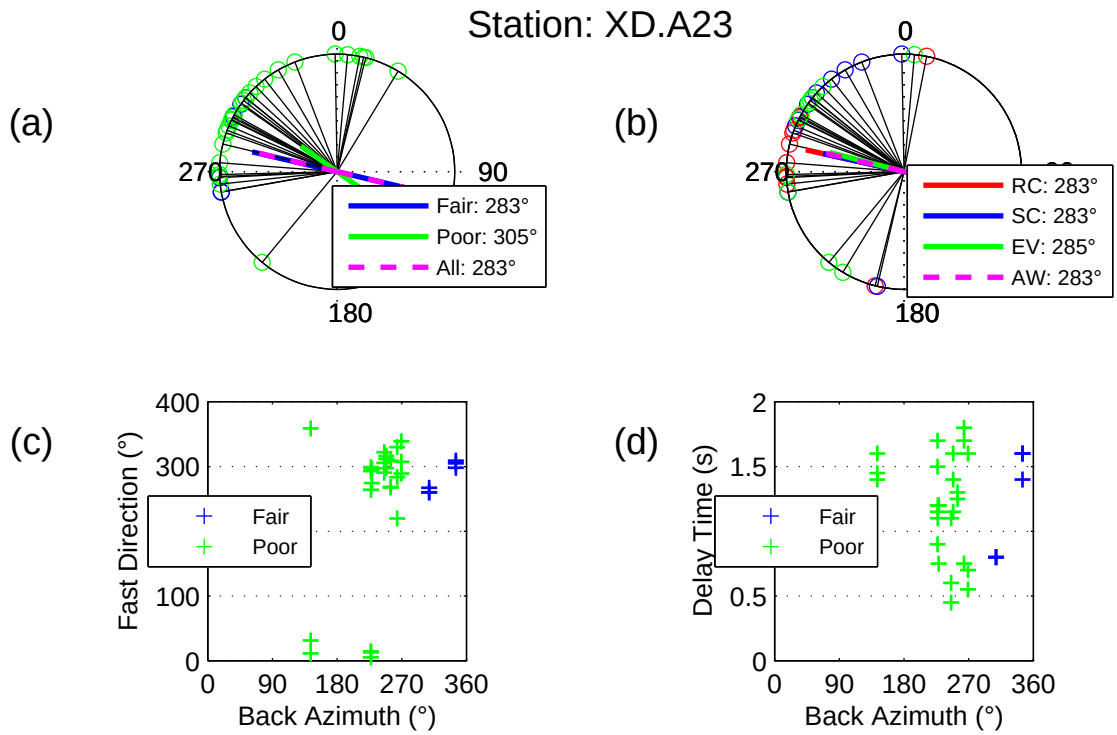

Figure DR29

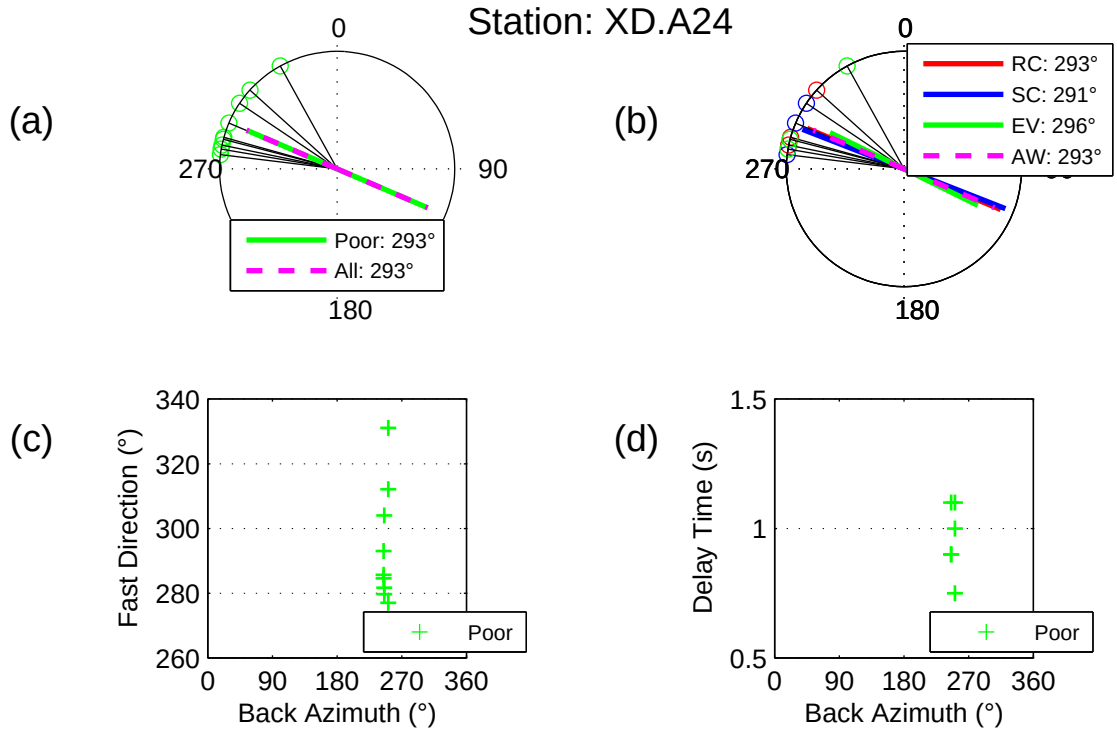

Figure DR30

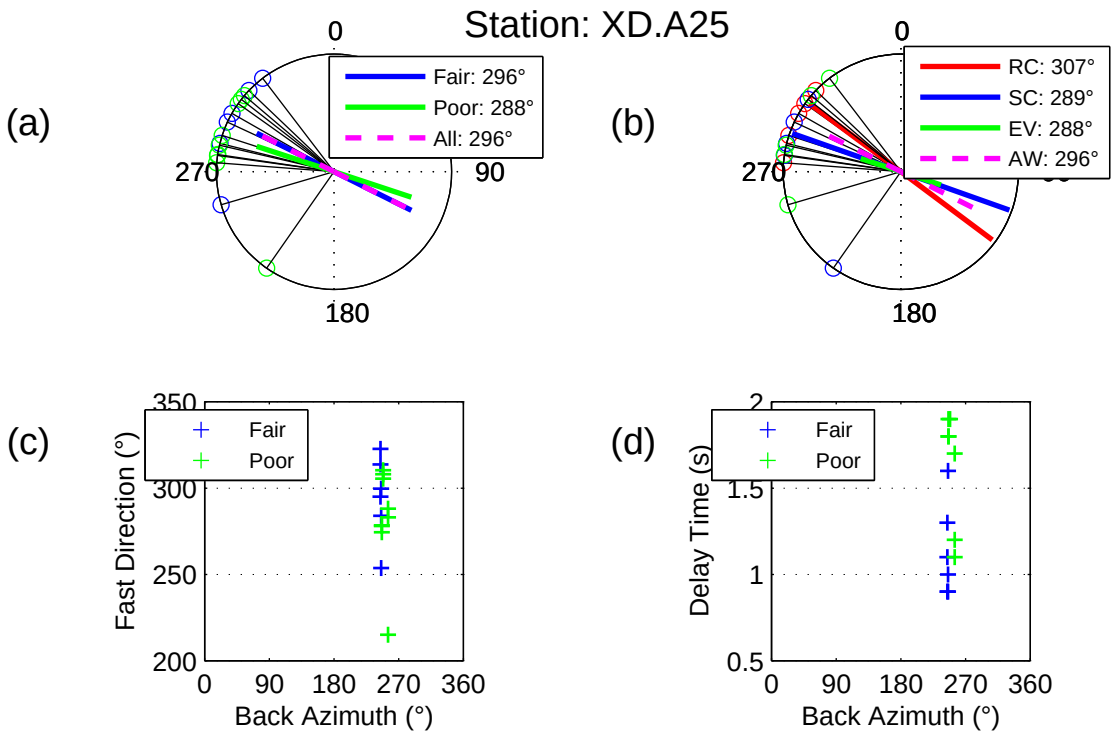

Figure DR31

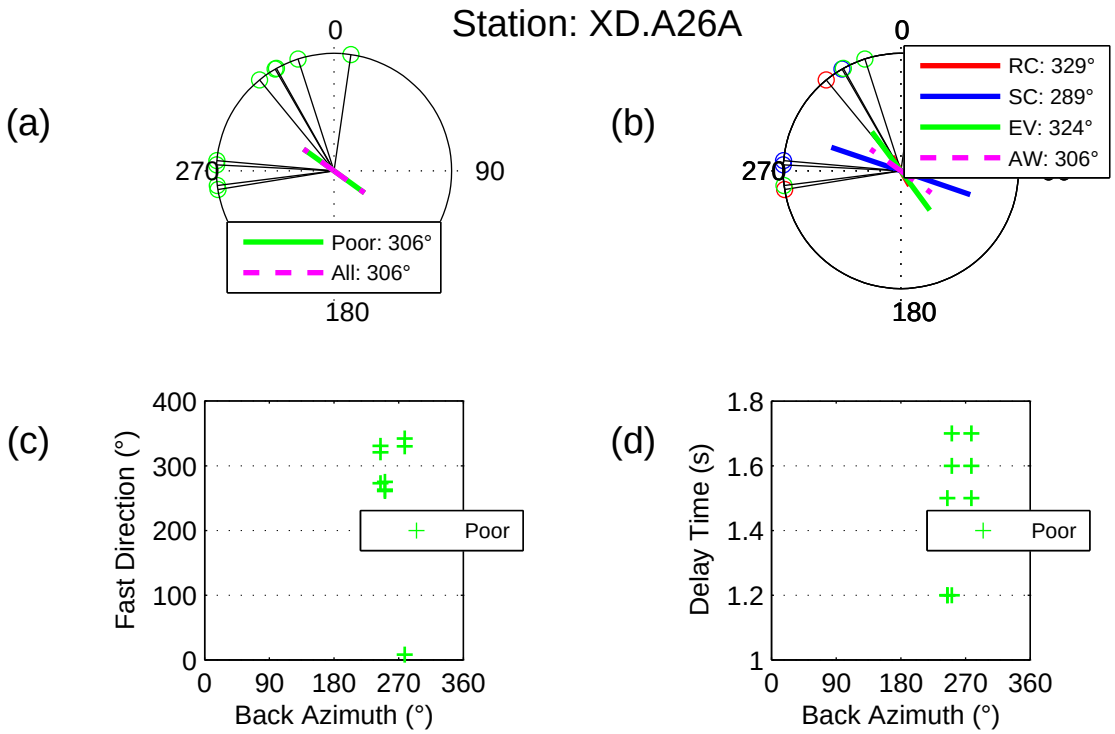

Figure DR32

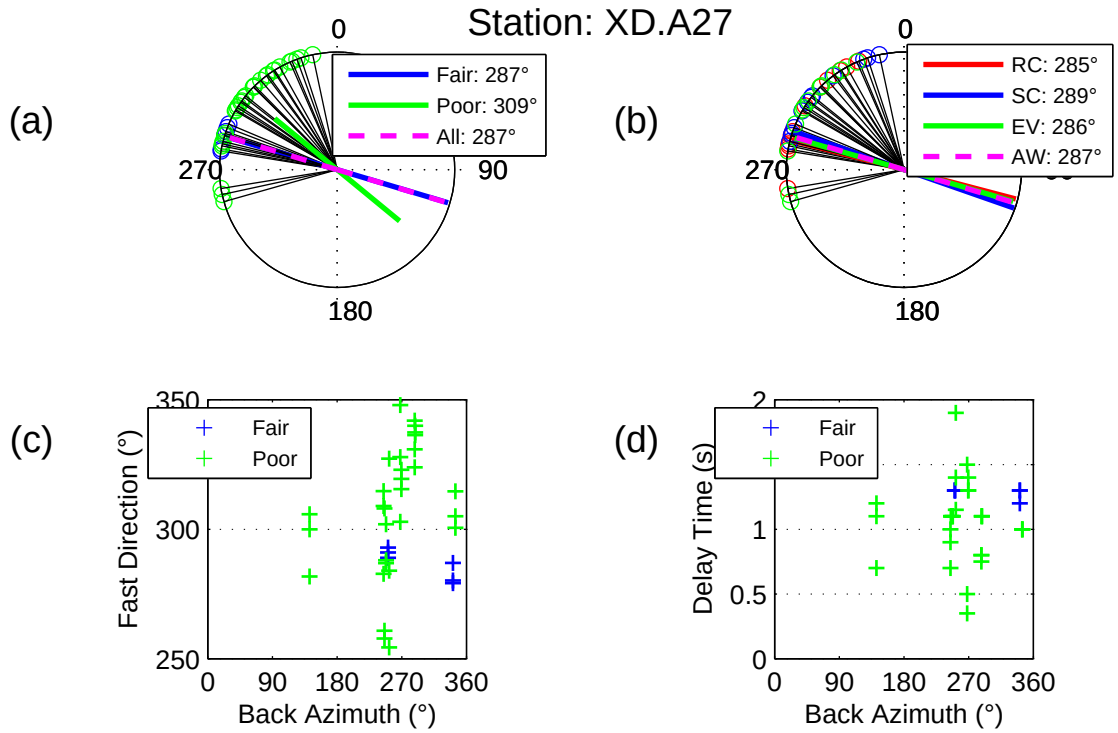

Figure DR33

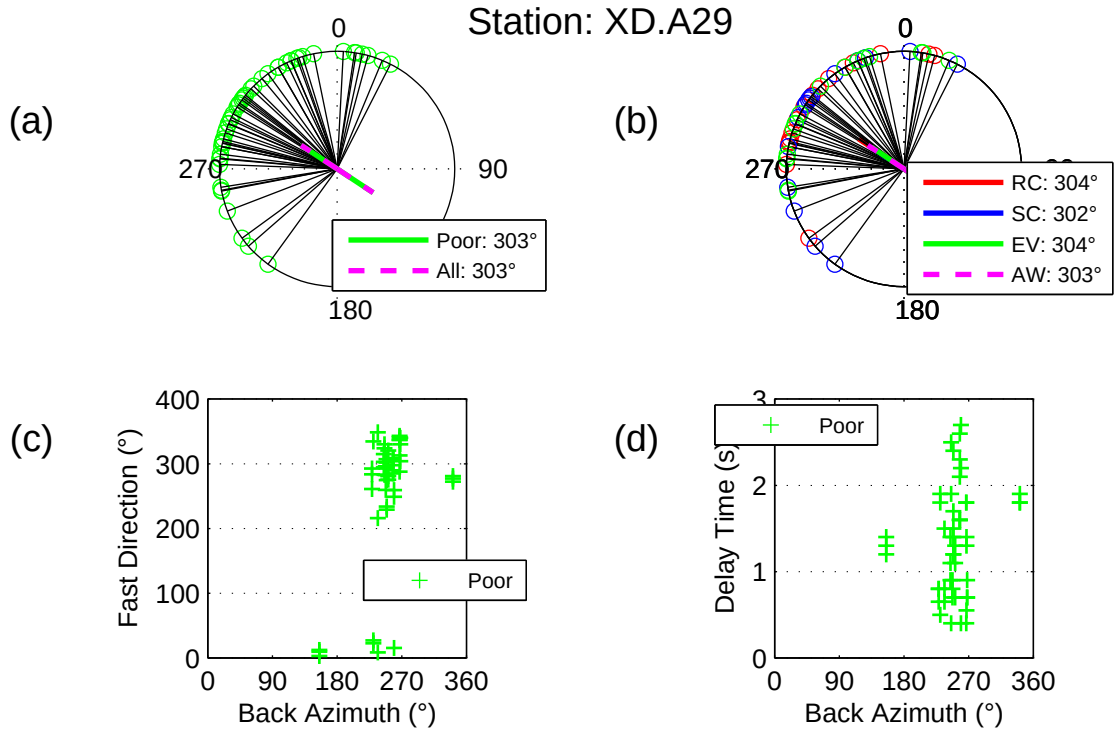

Figure DR34

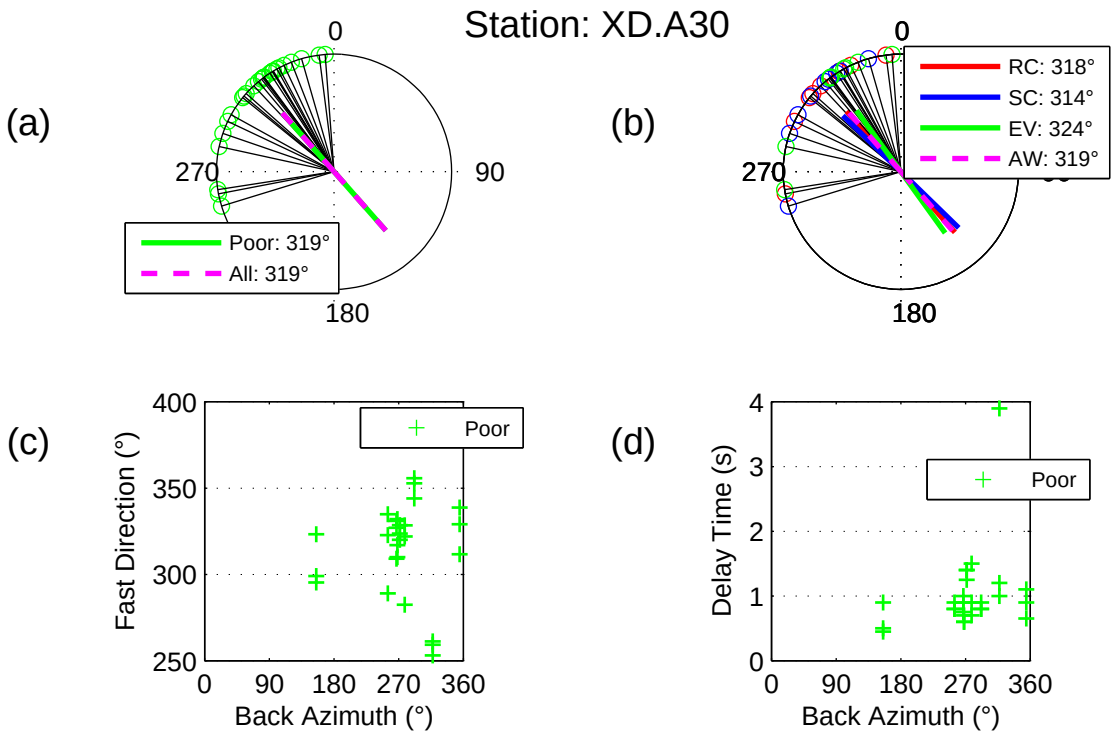

Figure DR35

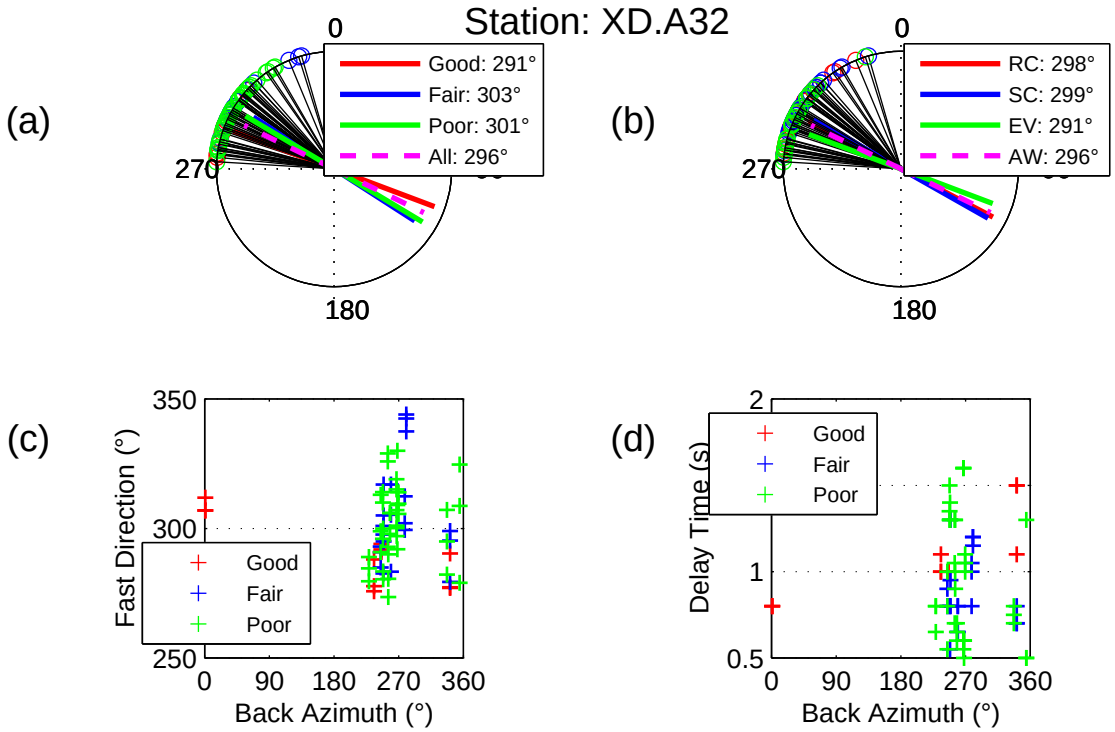

Figure DR36

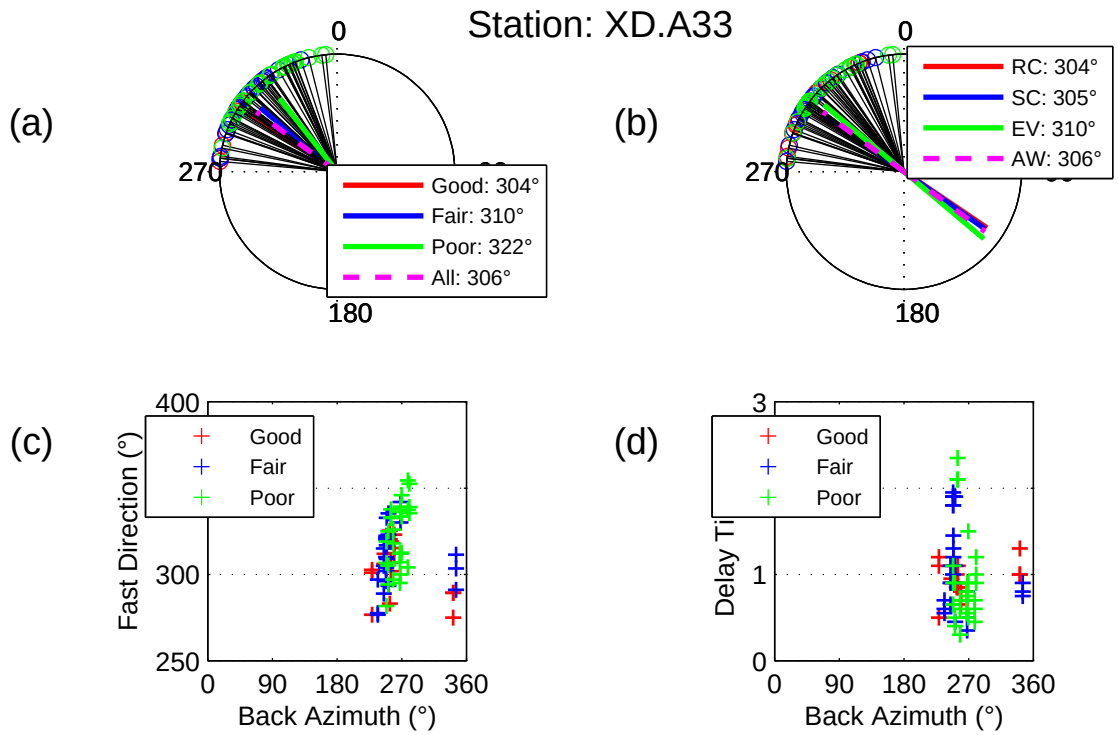

Figure DR37

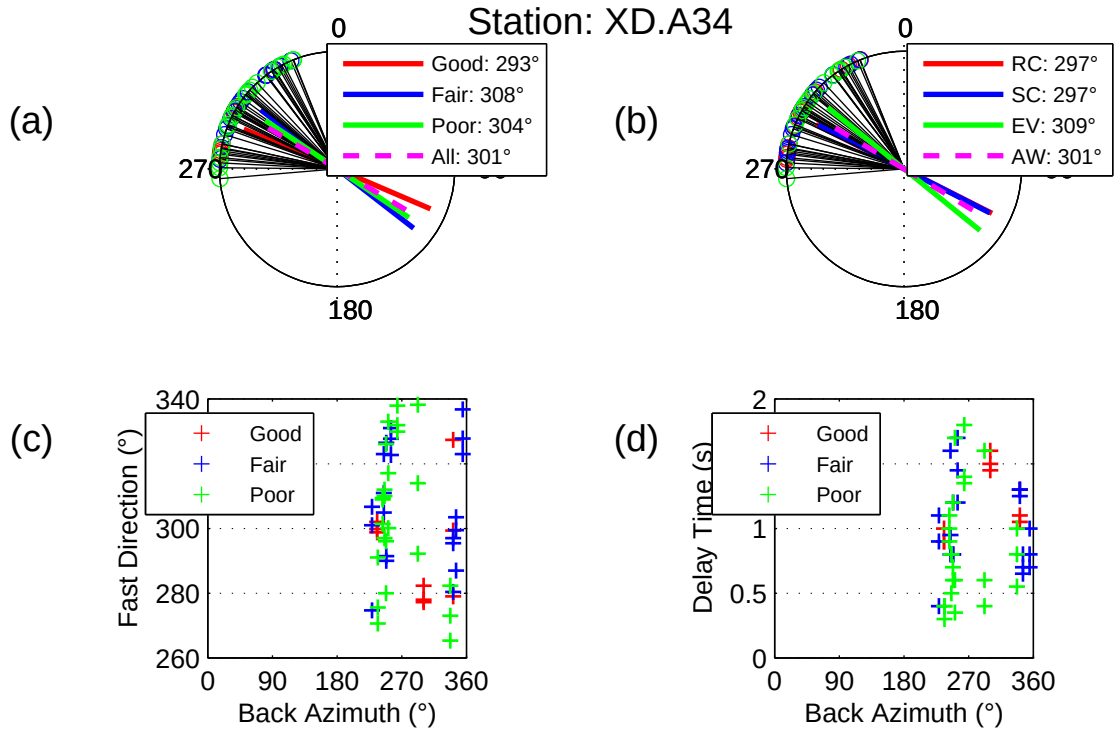

Figure DR38

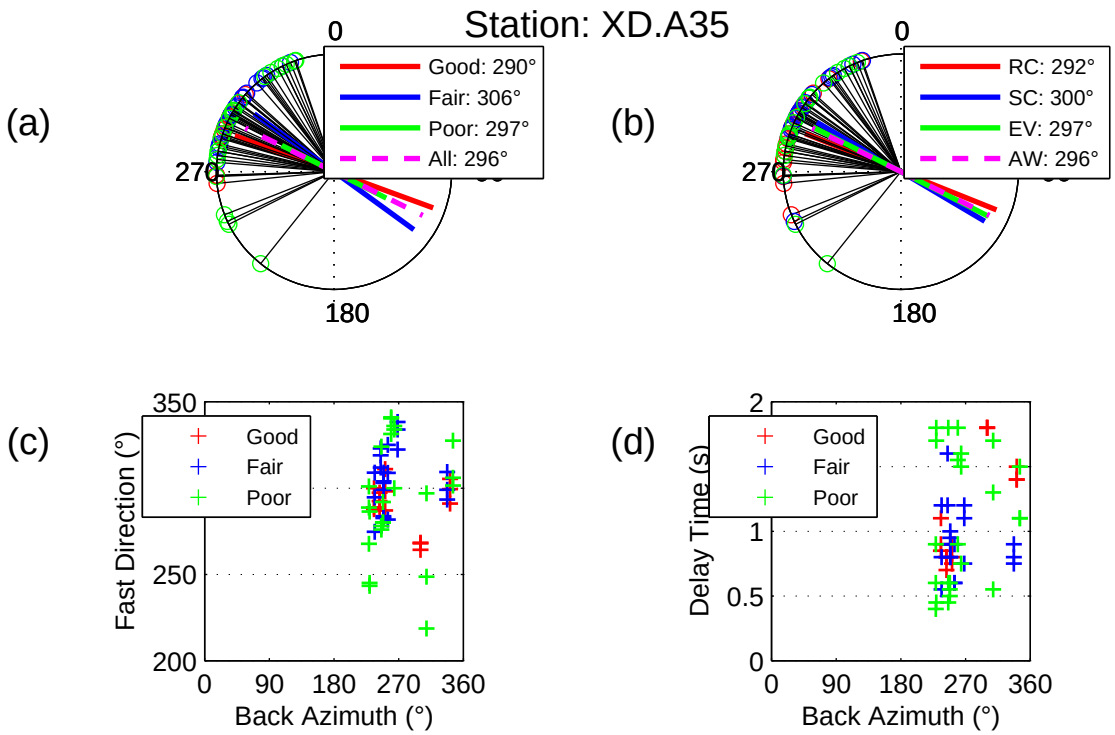

Figure DR39

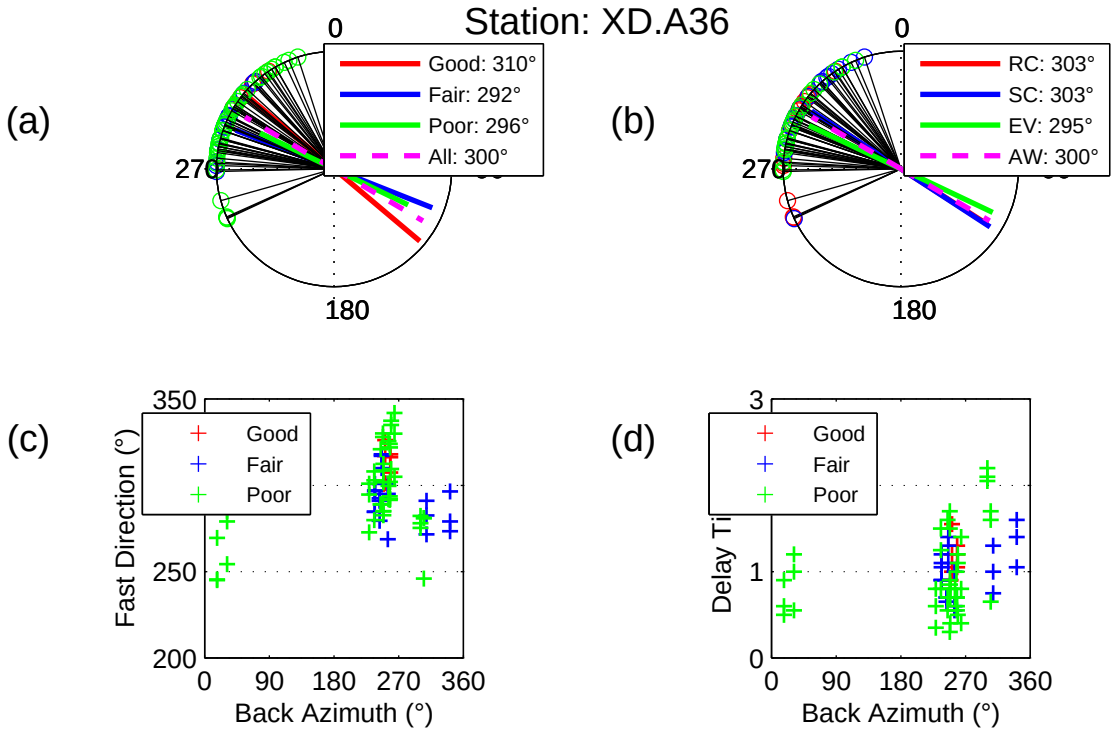

Figure DR40

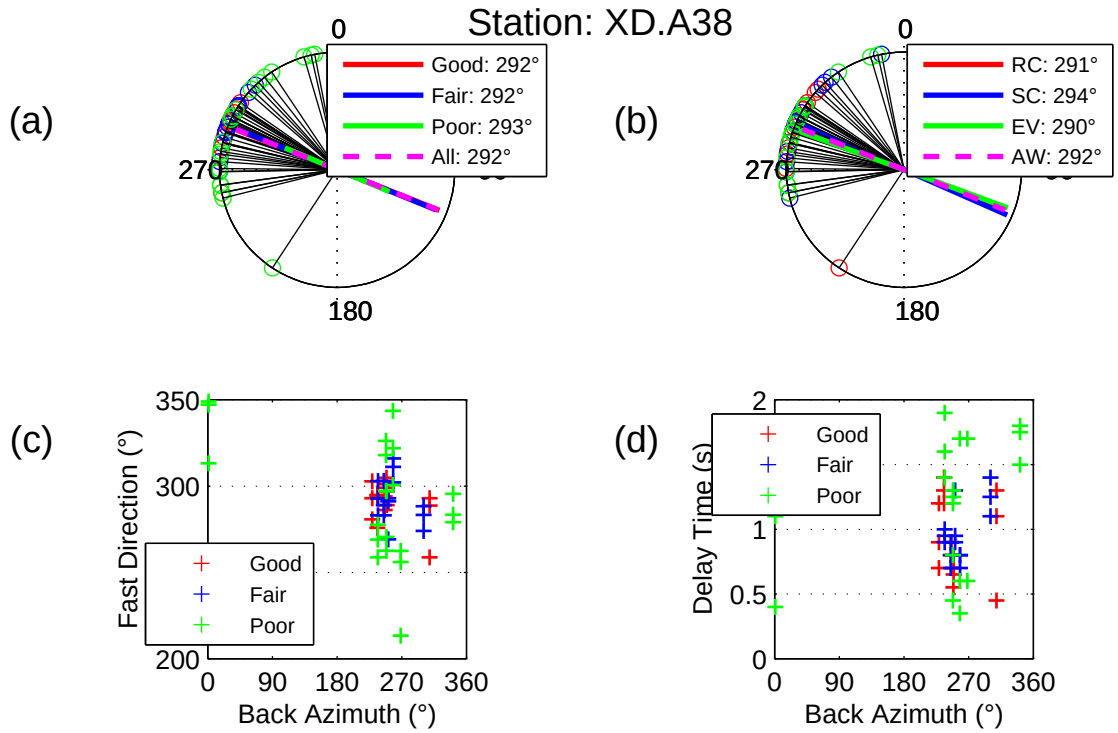

Figure DR41

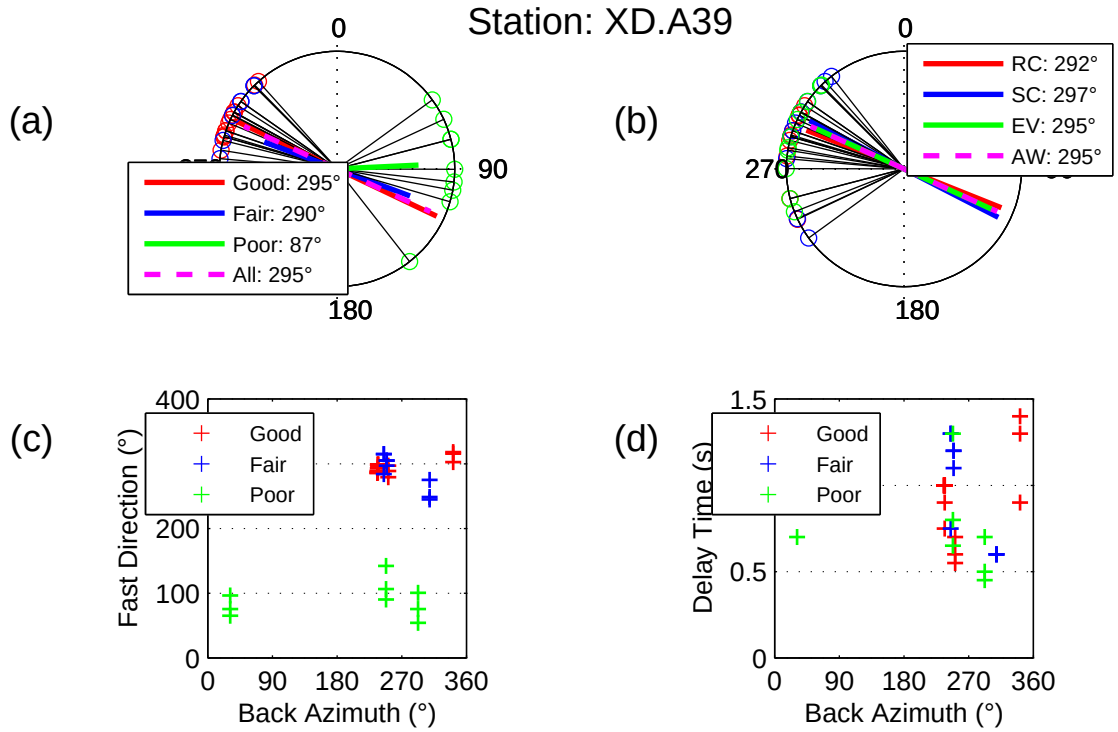

Figure DR42

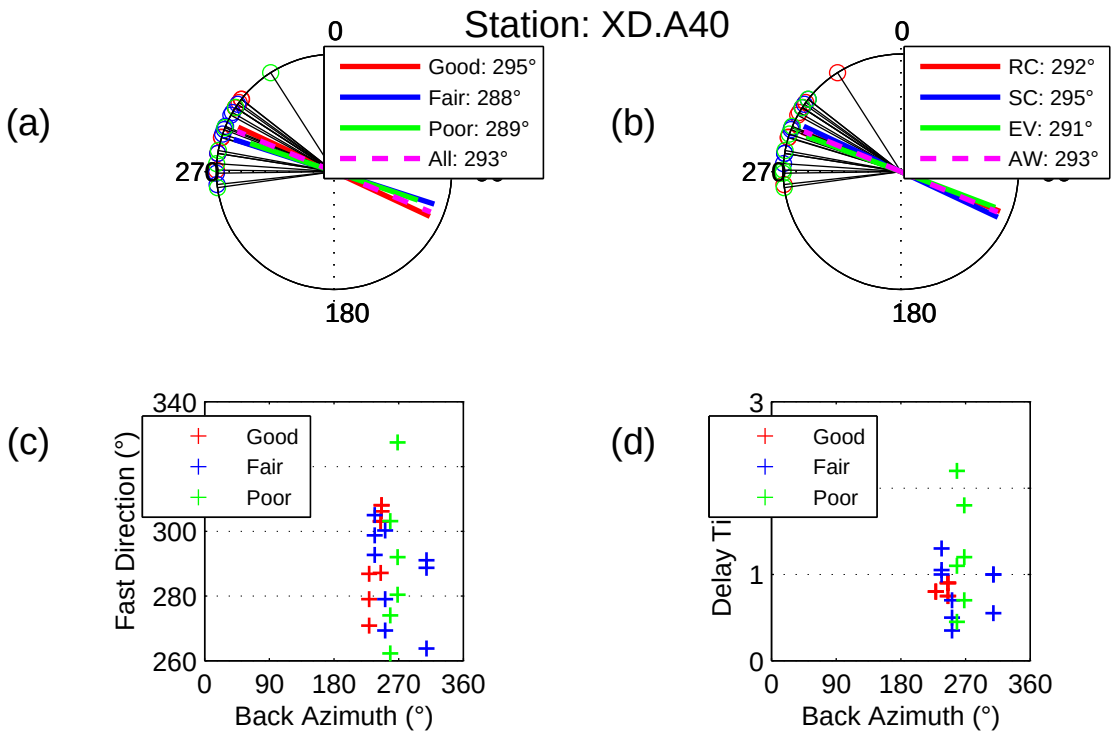

Figure DR43

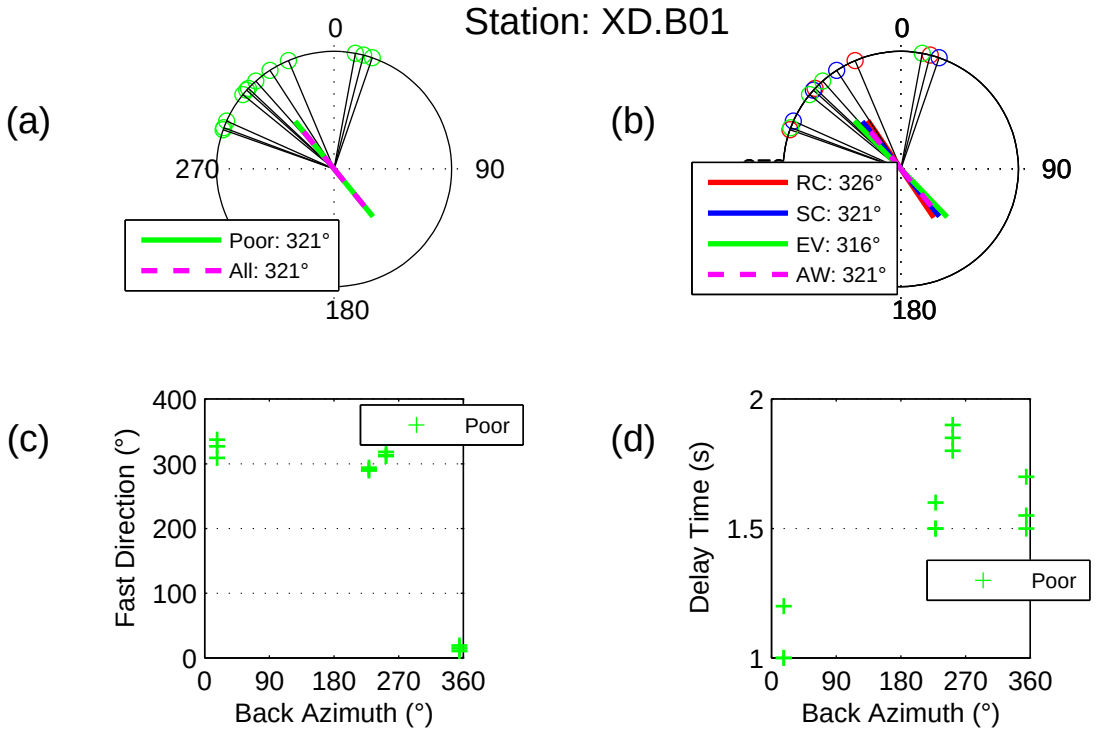

Figure DR44

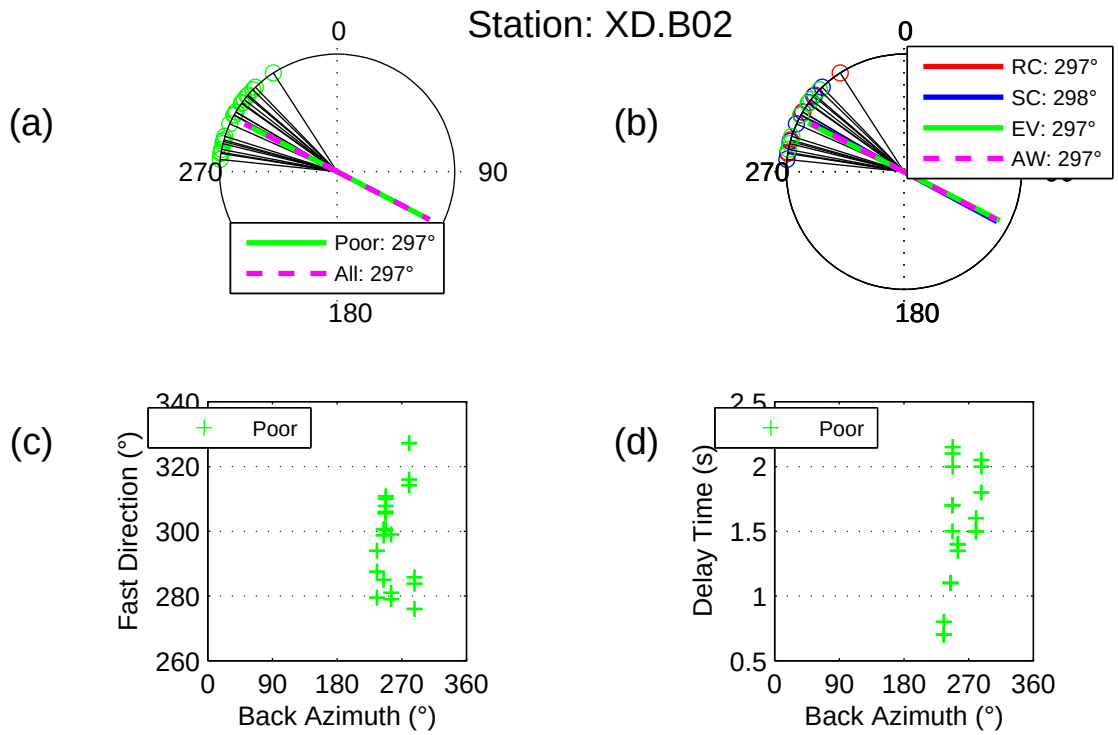

Figure DR45

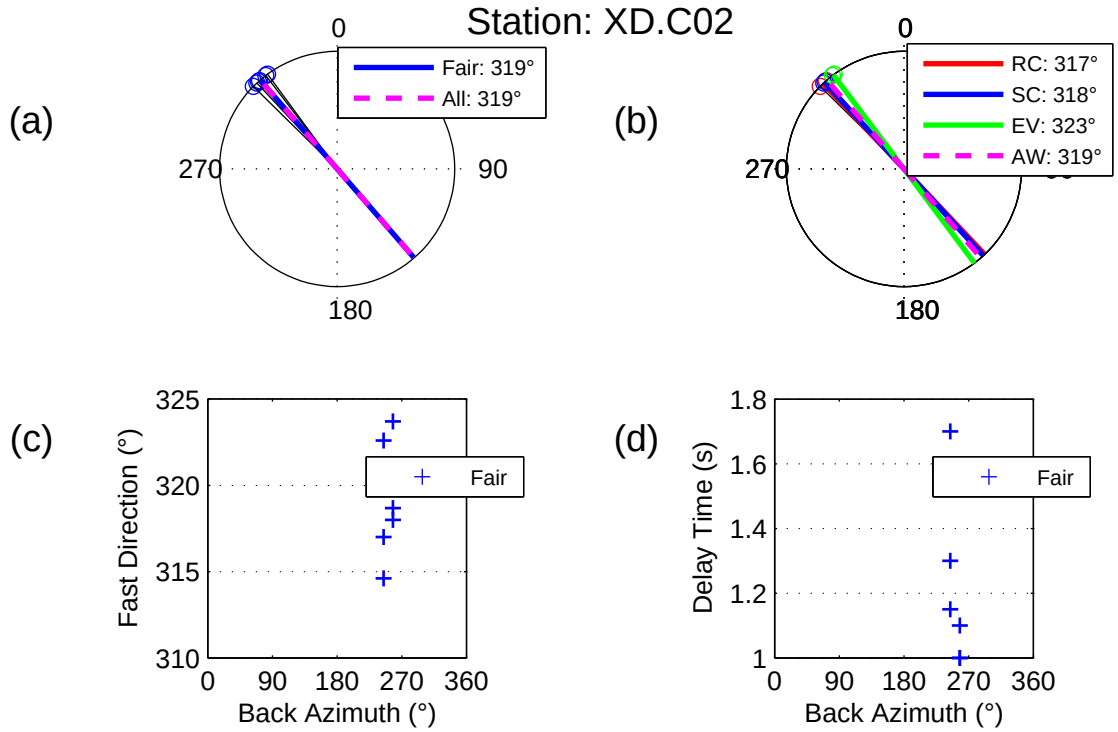

Figure DR46

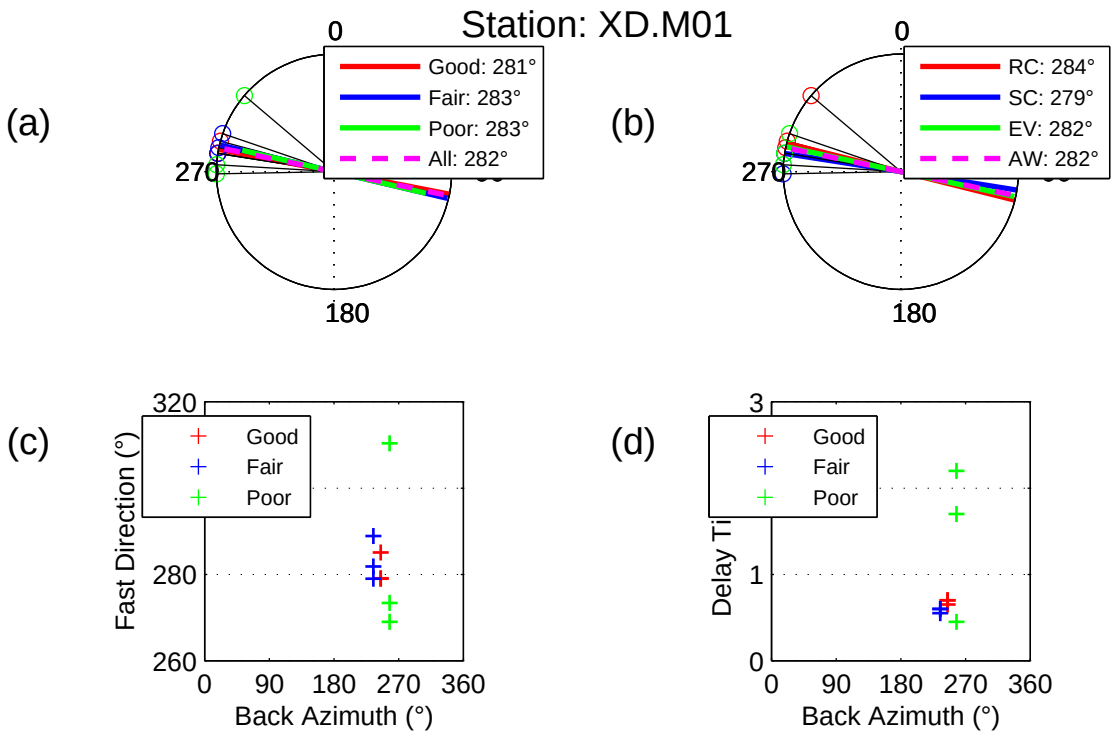

Figure DR47

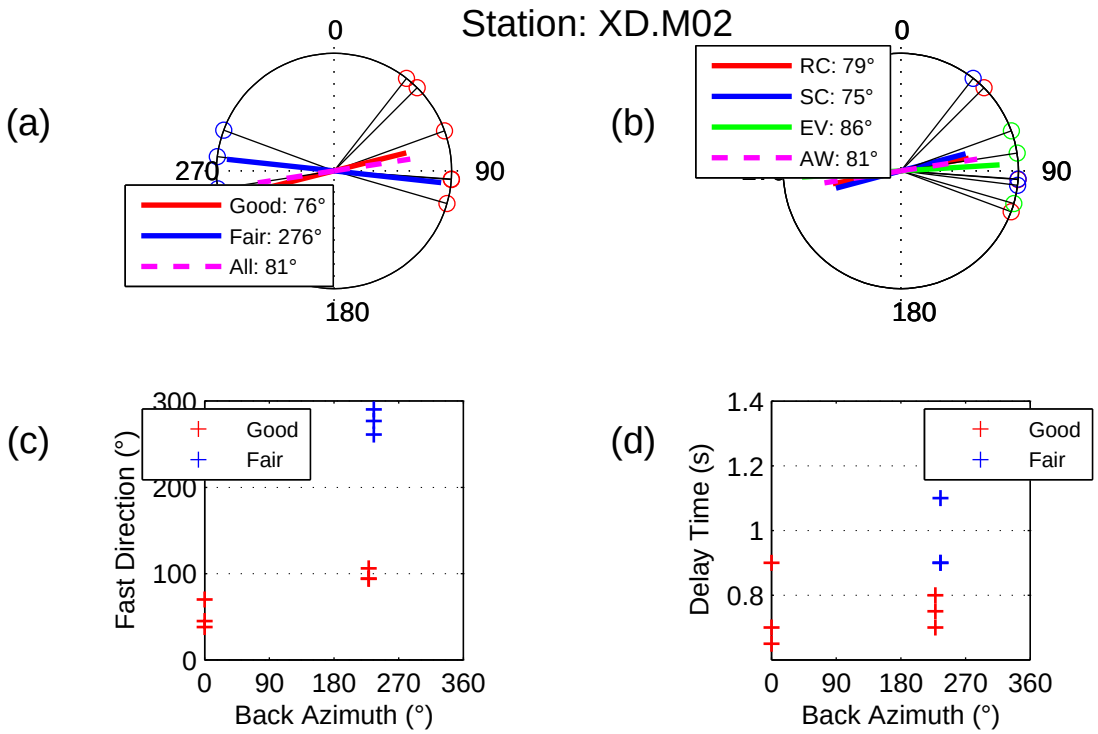

Figure DR48

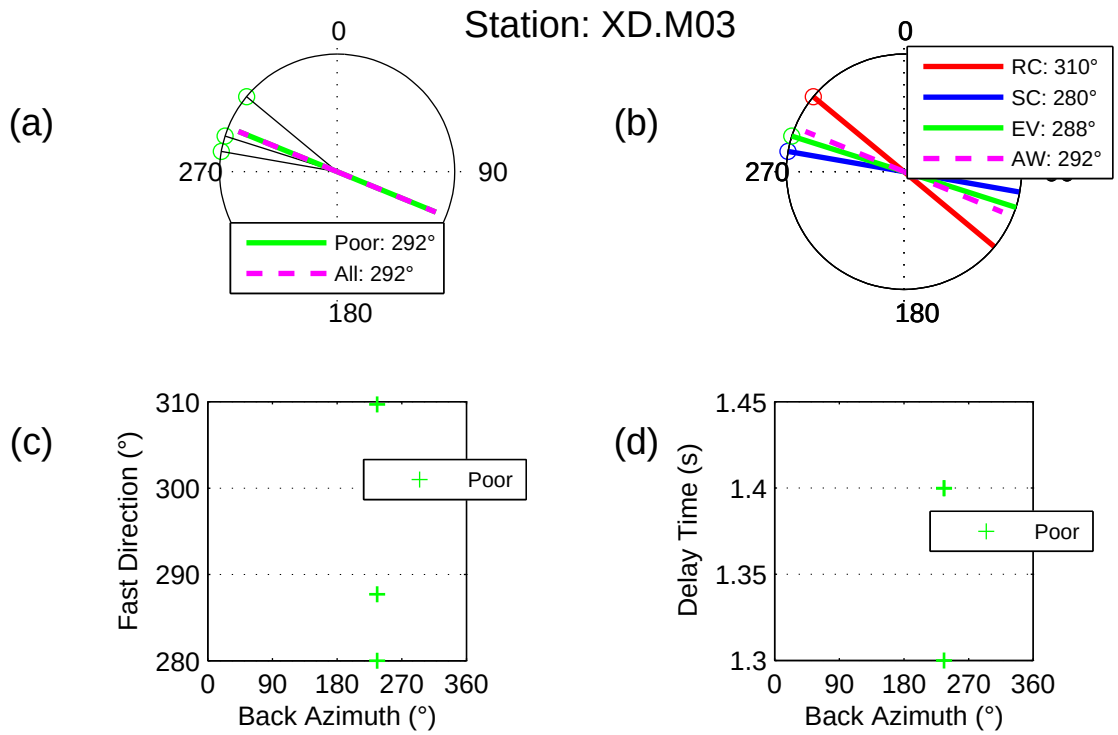

Figure DR49

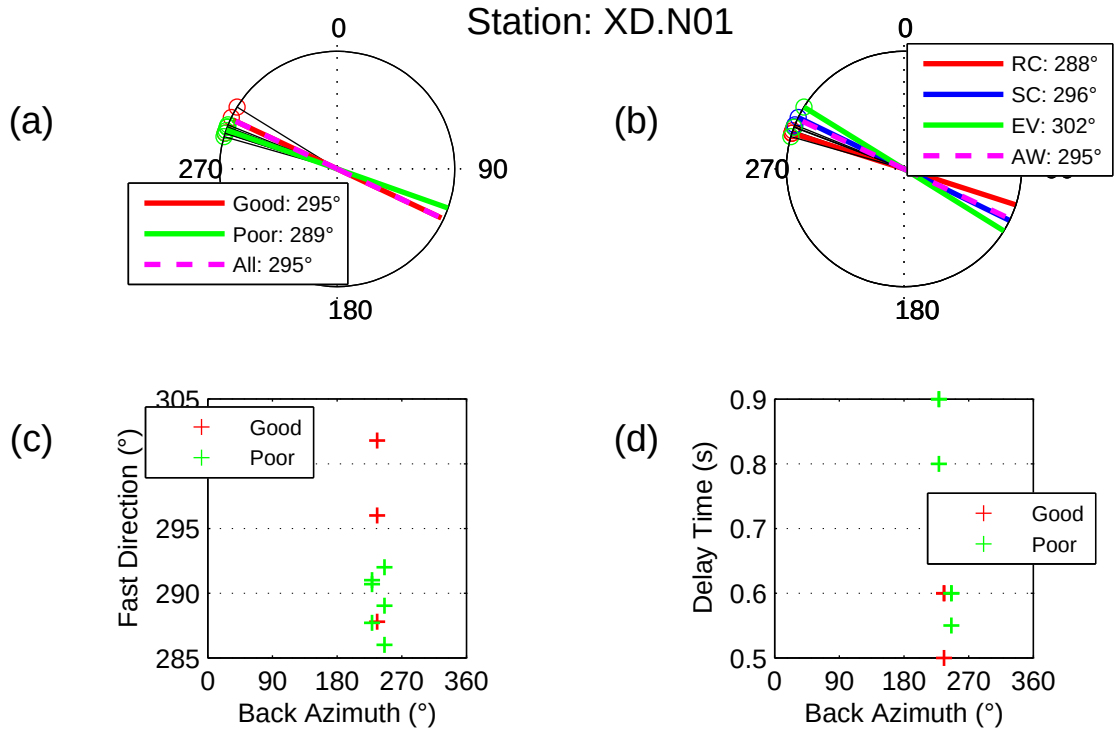

Figure DR50

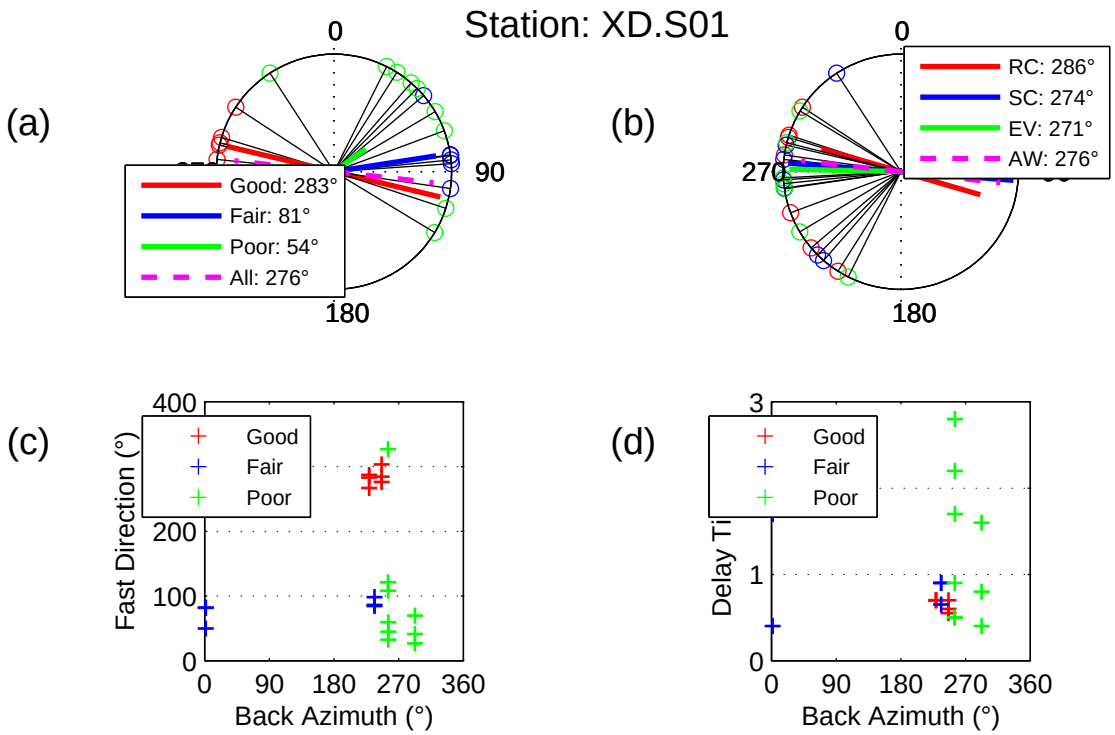

Figure DR51

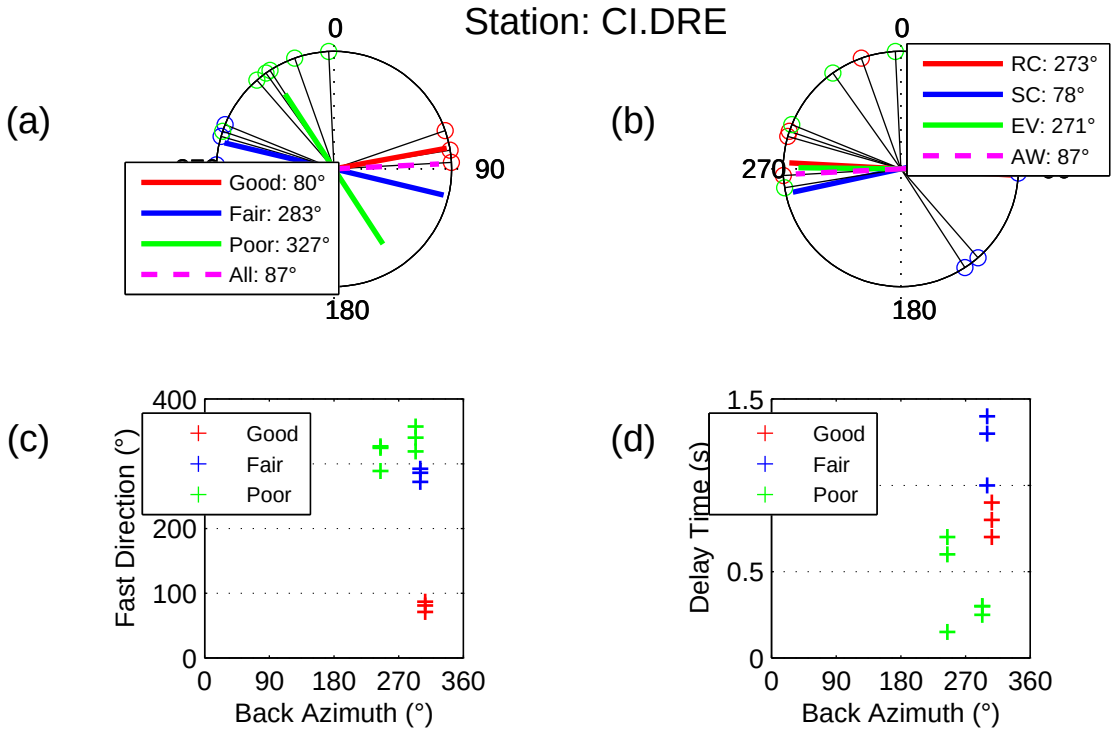

Figure DR52

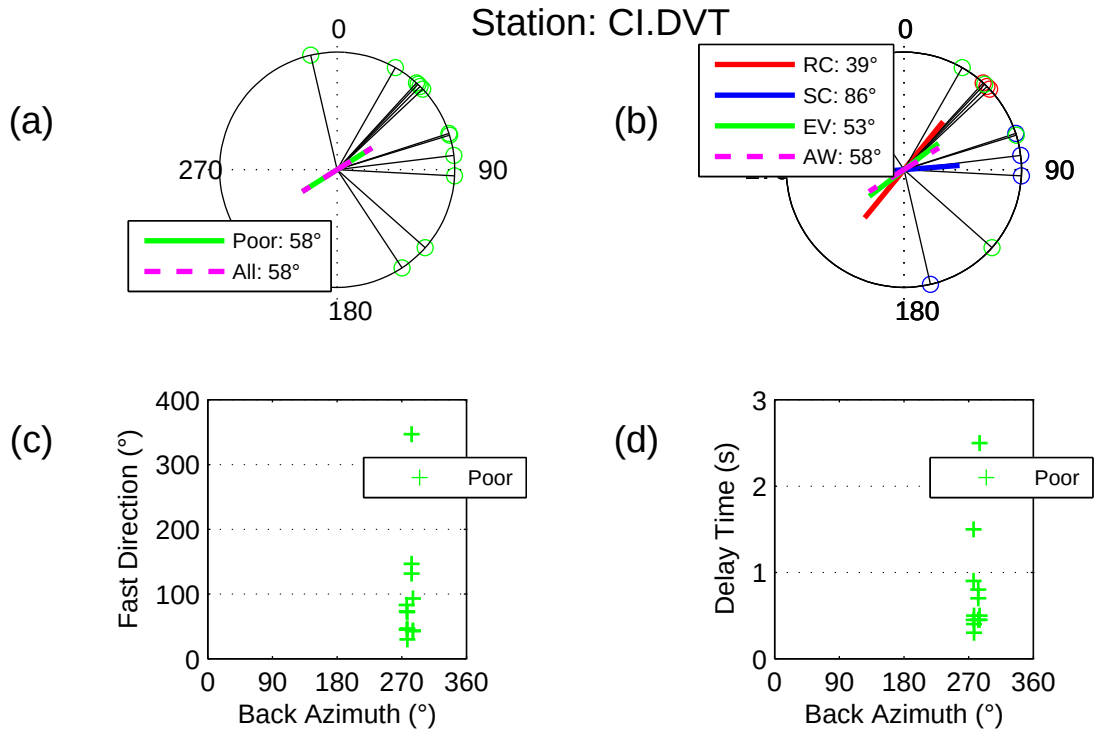

Figure DR53

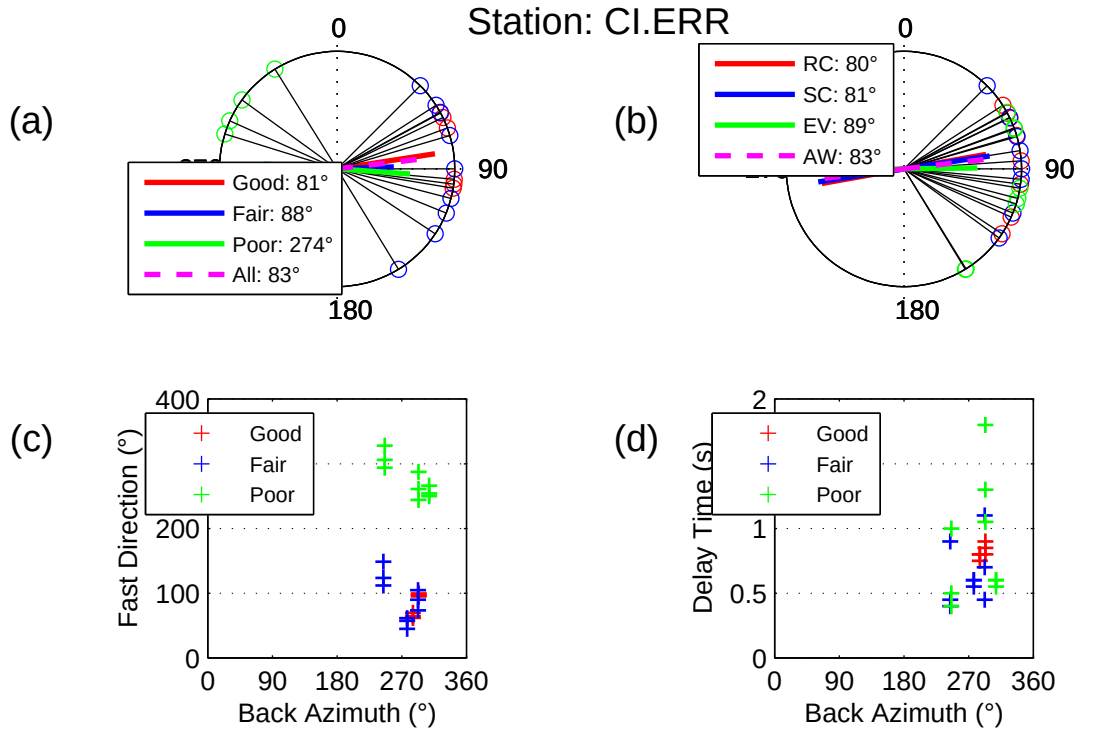

Figure DR54

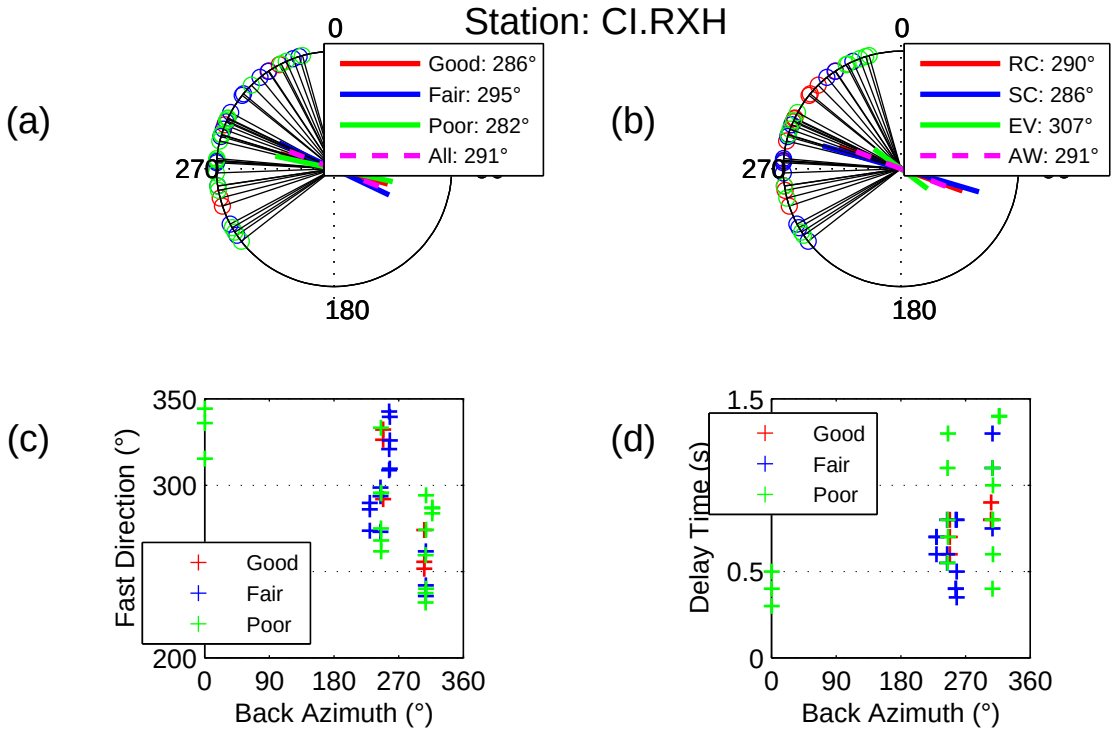
Station: CI.RXH
(a)
0
270
180
Good: 286°
Fair: 295°
Poor: 282°
All: 291°
(b)
0
270
180
RC: 290°
SC: 286°
EV: 307°
AW: 291°
(c)
350
300
200
Fast Direction (°)
Good
Fair
Poor
0 90 180 270 360
Back Azimuth (°)
(d)
1.5
0.5
0
Delay Time (s)
Good
Fair
Poor
0 90 180 270 360
Back Azimuth (°)

Figure DR55

Table DR1: Mean splitting parameters for geographic domains defined in Figure 2.

	N	ϕ_m	δt_m	Station Names
PRB	17	79 ± 14	0.8 ± 0.15	A01-A13, M01, M02, CBX, NE71
ST	23	124 ± 19	1.0 ± 0.25	A14-A16, A18-A27, A29, A30, A32, B01, B02, C02, M03, RXH, DRE, NE70
ETR	11	117 ± 5	0.9 ± 0.14	A33-A36, A38-A40, N01, S01, GLA, 112A
BRP	6	76 ± 10	1.0 ± 0.33	BLY, Y12C, P36, 113A, Z13A, Y13A

N: Number of stations. ϕ_m: Axial-mean of fast polarization. δt_m: Mean delay time. PRB: Peninsular Ranges Batholith; ST: Salton Trough; ETR: Eastern Transverse Ranges; BRP: southern Basin-&-Range Province.

Table DR2: Comparison with previous splitting measurements.

Station	This Study	Previous Work*Monteiller and Chevrot* [2011]
RXH	$\bar{\phi} = 111 \pm 57$; $\bar{\delta t} = 0.72 \pm 0.20$	$\bar{\phi} = 101$; $\bar{\delta t} = 1.18$
DRE	$\bar{\phi} = 87 \pm 26$; $\bar{\delta t} = 0.94 \pm 0.23$	$\bar{\phi} = 103$; $\bar{\delta t} = 0.55$
DVT	$\bar{\phi} = 57 \pm 65$; $\bar{\delta t} = 0.78 \pm 0.60$	$\bar{\phi} = 43$; $\bar{\delta t} = 0.39$
ERR	$\bar{\phi} = 83 \pm 45$; $\bar{\delta t} = 0.74 \pm 0.17$	$\bar{\phi} = 76$; $\bar{\delta t} = 1.16$

$\bar{\phi}$: Axial-mean of fast polarization. $\bar{\delta t}$: Mean delay time.